J. Fluid Mech. (2005), *vol.* 543, *pp.* 303–331. © 2005 Cambridge University Press
doi:10.1017/S0022112005006476 Printed in the United Kingdom

Regimes of drop morphology in oblique impact on deep fluids

By G. LENEWEIT[1,2], R. KOEHLER[2], K. G. ROESNER[1] AND G. SCHÄFER[2]

[1]Department of Fluid Mechanics and Aerodynamics, Technical University of Darmstadt,
Petersenstr. 30, D-64287 Darmstadt, Germany

[2]Carl Gustav Carus-Institut der Gesellschaft zur Förderung der Krebstherapie e.V.,
Am Eichhof 30, D-75223 Niefern-Öschelbronn, Germany

(Received 2 September 2003 and in revised form 20 June 2005)

Oblique impact of single drops on deep fluids at various impact angles α is studied for a wide Weber number range ($15 \leqslant We \leqslant 249$), where α is varied between 5.4° and 64.4° with respect to the target surface, and drop and target consist of the same fluid (water/glycerol). In the range of studied parameters, coalescence always takes place. Below a critical level of the Weber number We_N formed with the normal velocity component, $We_N < 10$, capillary waves are produced on the drop and target surface in the first stage after impact. For $We_N > 10$, a lamella is ejected from the target surface and drop volume for which both experimental and numerical evidence is given. For $We < 140$ and $\alpha < 23°$, the drop spreads on the target surface with no visible immersion of drop fluid into the target fluid. Outside this range, a partial immersion of drop fluid can be seen: for $We_N > 10$, it occurs in the front part of the spreading drop; for $\alpha > 23°$, in the rear part of the impact crater. The spreading patterns of the drop fluid are visualized with dyed drop fluid once it has come to rest after impact. In many cases, patterns of high complexity and strong sensitivity to the impact conditions can be seen which are very reproducible for similar impact conditions. The mechanisms underlying capillary wave or lamella formation and the partial immersions of drop fluid are discussed and their relevance for pattern formation is taken into account.

1. Introduction

Drop impact on surfaces plays a major role in many diverse fields of science, rendering it a fundamental fluid mechanical problem. The appearance of drop impact on fluids or solids ranges from agriculture (soil erosion, pesticide distribution), oceanography (oxygen absorption in water, noise generation), meteorology (cloud generation), astrophysics (meteorite impacts), to applications in mechanical and chemical engineering (fuel injection, spray coating, spray drying, pyrometallurgical operations, ink-jet printing). The work is motivated by the desire to elucidate the physical principles of many puzzling phenomena or to promote innovations in technological applications. Moreover, many workers describe the beauty of the phenomena observed.

There is extensive literature on many aspects of drop impact among which only the more recent will be cited. Impact on plain solid surfaces is studied by Yarin & Weiss (1995), Roisman, Rioboo & Tropea (2002) and Rioboo, Marengo & Tropea (2002); the movement of the contact or triple line for impact on solids by de Ruijter, De Coninck & Oshanin (1999) and Reznik & Yarin (2002). Morton, Rudman & Liow (2000) show numerical and Liow (2001), Manzello & Yang (2002) experimental results of normal impact on deep fluids, whereas Wang & Chen (2000) are occupied with impacts on films. The formation of a 'lamella' or 'ejecta sheet' is examined by Thoroddsen (2002), crown formation by Weiss & Yarin (1999) and Roisman & Tropea (2002) and capillary effects at liquid–liquid contacts by Rein (2002*a*). Binary droplet collisions are investigated by Qian & Law (1997), Willis & Orme (2000) and Beard, Ochs & Liu (2001). Results on oblique drop impact on solid surfaces are reported by Bussmann, Mostaghimi & Chandra (1999) and Kang & Lee (2000). Overviews on different aspects of drop–surface interactions are given by Rein (1993) and Rein (2002*b*).

Compared to the detailed investigations mentioned above, oblique drop impact on deep fluid pools has received little attention in recent years. In order to understand the process of cloud formation Schotland (1960), Jayaratne & Mason (1964), Zhbankova & Kolpakov (1990, 1999) determined the regimes for rebounding and coalescence in the low-Weber-number range ($0.1 \leqslant We \leqslant 4$) for different impact angles α ($10^\circ \leqslant \alpha \leqslant 90^\circ$). All authors found a threshold Weber number $We_{crit}(\alpha)$ between rebounding ($We < We_{crit}$) and coalescence ($We > We_{crit}$) with $0.8 \leqslant We_{crit}(\alpha) \leqslant 3$. For small We, the droplets rebound as long as the separating gas layer is not overcome by attractive van der Waals forces which is supposed to occur for distances $< 50\,\mathrm{nm}$ as shown by MacKay & Mason (1963).

There is only one investigation of oblique drop impact at higher We ($7 \leqslant We \leqslant 60$) reported by Ching, Golay & Johnson (1984). They study both single and periodic drop impacts at different α and find regimes for rebounding and coalescence for periodic impacts, but never observe single drops to rebound. They do not report how many impacts of a single drop are studied and their respective parameters (We, α). Also, no further details after coalescing impact are described.

Periodic drop impacts are easier to visualize since no high-speed recording is required, but they introduce random errors: Zhbankova & Kolpakov (1990) state that the regimes found for rebounding and coalescence for periodic drops could only be expressed in terms of probabilities, presumably because of the perturbations produced (surface waves on the target surface) which make boundary conditions for impact undefined. Therefore, consistent data for the regimes of rebounding, coalescence or splashing can only be obtained using single drops. To the best of our knowledge, no results can be found in the literature concerning the deformation of drop fluid after coalescing oblique impact and its spreading on the target surface or mixing with target fluid. These questions are the main concern of the present study. Moreover, rebounding after initial coalescence found in this study is briefly summarized.

2. Experimental and numerical methods

Single drops with diameter D were generated by a nozzle of diameter 0.6 mm connected to a pressure chamber with a maximum diameter of 25 mm and a volume of 20 ml closed with a rubber membrane at the rear, which was compressed and immediately released with a magnetic coil (see figure 1*b*). Short currents in a time interval of 0.4 to 0.8 ms from a $500\,\mu\mathrm{F}$ condensor at $7-40\,\mathrm{V}$ produced drops with diameters D in the range $1.45\,\mathrm{mm} \leqslant D \leqslant 2.0\,\mathrm{mm}$ and a reproducibility of $\pm 3\%$ for D with identical parameters of the drop generator. At higher drop velocities $u \geqslant 2.5\,\mathrm{m\,s^{-1}}$

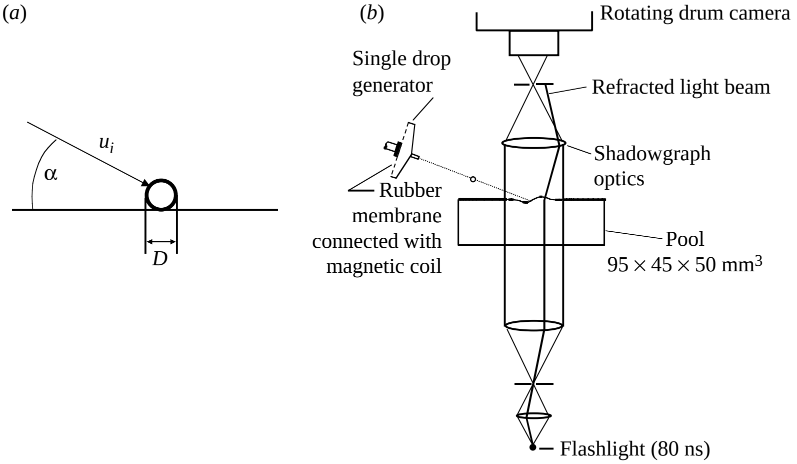

FIGURE 1. (*a*) Sketch of parameters of the impact geometry. (*b*) Experimental set-up.

fluid jets were often ejected that disintegrated into multiple drops; for $u < 2.5\,\mathrm{m\,s^{-1}}$ mostly single drops were produced.

The drops impacted at the liquid surface of a pool of dimensions $95 \times 45 \times 50\,\mathrm{mm}$ (length × width × depth) at an impact angle α and an impact velocity u_i, as depicted in figure 1(*a*). Both the drop and the target fluid consisted of a glycerol/water mixture with 61% of glycerol (w/w), density $\rho = 1157\,\mathrm{kg\,m^{-3}}$ and kinematic viscosity $\nu = 10\,\mathrm{mm^2\,s^{-1}}$. The glycerol/water mixture with its specific viscosity was chosen to simulate the impact of smaller water drops in the same Weber- and Reynolds-number range according to the laws of hydrodynamic similarity. Moreover, the Reynolds-number range chosen here ($116 \leqslant Re \leqslant 534$) fits well into the ranges covered by previous studies on oblique impact, e.g. Schotland (1960) with Re being in the range of 100 to 400; Jayaratne & Mason (1964) with $30 \leqslant Re \leqslant 260$; Ching *et al.* (1984) with $550 \leqslant Re \leqslant 1210$ and Zhbankova & Kolpakov (1999) with $40 \leqslant Re \leqslant 140$.

The drop fluid was dyed with bromothymol blue with a concentration of 3×10^{-4} (w/w) which did not influence the surface tension $\sigma = 67.3\,\mathrm{mN\,m^{-1}}$ being identical for both the drop and target fluid. Drop and target fluid were kept at ambient temperature, i.e. $21 \pm 1\,^{\circ}\mathrm{C}$.

Drop impact and the spreading of drop fluid on the target fluid surface were visualized with shadowgraph optics, as shown in figure 1(*b*). Flashlight illumination was produced by a Nanolite® lamp (High-Speed Photo-Systeme, Wedel, Germany) with a flash duration of 80 ns (half-width). Visualizations were recorded with a high-speed rotating drum camera (Zeiss, Oberkochen, Germany) with at most $10\,600\,\mathrm{frames\,s^{-1}}$ on a 35 mm b/w film with a frame width of 9 mm. Two objectives with $f = 320\,\mathrm{mm}$, diameter $= 80\,\mathrm{mm}$ were used for the shadowgraph optics, the camera objective had a focal length $f = 90\,\mathrm{mm}$. Drop impact visualizations could be taken alternatively either in vertical perspective with illumination from below the pool or in lateral perspective. The usual recording interval was set to 0.42 ms in lateral and 0.94 ms in vertical perspective in order to record the full event in a series of 60 frames with a sufficient time resolution. In vertical perspective, the dynamics could be traced longer than in the lateral perspective, where at the end of the series the target surface appeared as a straight line, therefore the recording rate had to be chosen longer for the vertical perspective. To eliminate distortion caused by a meniscus at the pool

Dimensionless group	Ranges covered
$We = \rho u_i^2 D/\sigma$	$15 \leqslant We \leqslant 249$
$We_N = \rho u_{i,N}^2 D/\sigma$	$0.7 \leqslant We_N \leqslant 70.2$
$Re = u_i D/\nu$	$116 \leqslant Re \leqslant 534$
$Fr = u_i^2/(Dg)$	$34 \leqslant Fr \leqslant 363$

TABLE 1. Definitions of dimensionless groups and ranges covered.

walls, the horizontal rim of the glass walls was coated with paraffin wax. To that aim, paraffin wax was heated above its melting point of 57 °C and spread on the glass rim. After solidification at room temperature (21 ± 1 °C), the pool was filled exactly to the rim resulting in a contact angle of approximately 90° with respect to the vertical glass wall.

In lateral perspective, α, D and the impact velocity u_i could be evaluated directly from the photographs (by means of the last ten pictures before impact, whenever possible). In vertical perspective, α and u_i had to be evaluated taking into account the horizontal and vertical distance between nozzle and location of impact and the influence of gravity and air friction according to an approximation reported by A. Kaskas, see Brauer (1971).

The impact velocity u_i and the impact angle α were the two parameters to be varied over a wide range, whereas D was roughly constant ($1.45\ \text{mm} \leqslant D \leqslant 2.0\ \text{mm}$). All fluid parameters ν, ρ and σ were kept exactly constant in all experiments. For the impact of single drops the following parameter ranges of u_i and α were covered: $0.73\ \text{m s}^{-1} \leqslant u_i \leqslant 2.67\ \text{m s}^{-1}$; $5.4^\circ \leqslant \alpha \leqslant 64.4^\circ$. The ranges of the Weber, Reynolds and Froude numbers, We, Re and Fr are shown in table 1, where g is the acceleration due to gravity. For some dynamical processes during impact, the normal component $u_{i,N} = u_i \sin \alpha$ and the corresponding Weber number We_N are used, rather than the magnitude of the impact velocity u_i.

In the presentation of the results, the time t after impact is normalized to yield the dimensionless time $\tau = t u_i / D$. All length scales are normalized with the drop diameter D and all velocities with u_i.

Numerical simulations with the commercial CFD code FLUENT 6.0 were performed on a PC with two parallel Pentium3 processors. Drop and target fluid and the surrounding gas were modelled as three separate phases with the volume of fluid method (VOF), taking into account viscosity, but ignoring surface tension. All other material parameters are defined identically as in the experiments, i.e. fluid density $\rho = 1157\ \text{kg m}^{-3}$ and fluid viscosity $\nu = 10\ \text{mm}^2\ \text{s}^{-1}$ for both drop and target fluid; atmospheric pressure of gas phase: 1013 hPa; gas density: $1.2\ \text{kg m}^{-3}$, gas viscosity $\nu_g = 15.8\ \text{mm}^2\ \text{s}^{-1}$.

For the study of vertical impact, a two-dimensional axisymmetric grid with an axial length of 4.2 mm and a radial length of 2.4 mm was used. The drop had a radius of 1.2 mm and impacted on a target film with a thickness of 0.6 mm. As proved by comparison to experiments, a liquid film was sufficient for the simulation of the very first stage of impact. The initial distance of the drop from the target was 0.12 mm, the grid had a maximal resolution in the vicinity of the film surface of 1.2 μm; the whole grid contained 19200 cells. The equations of continuity and momentum were solved in time steps $\Delta\tau = 10^{-7}$ where good convergence was obtained.

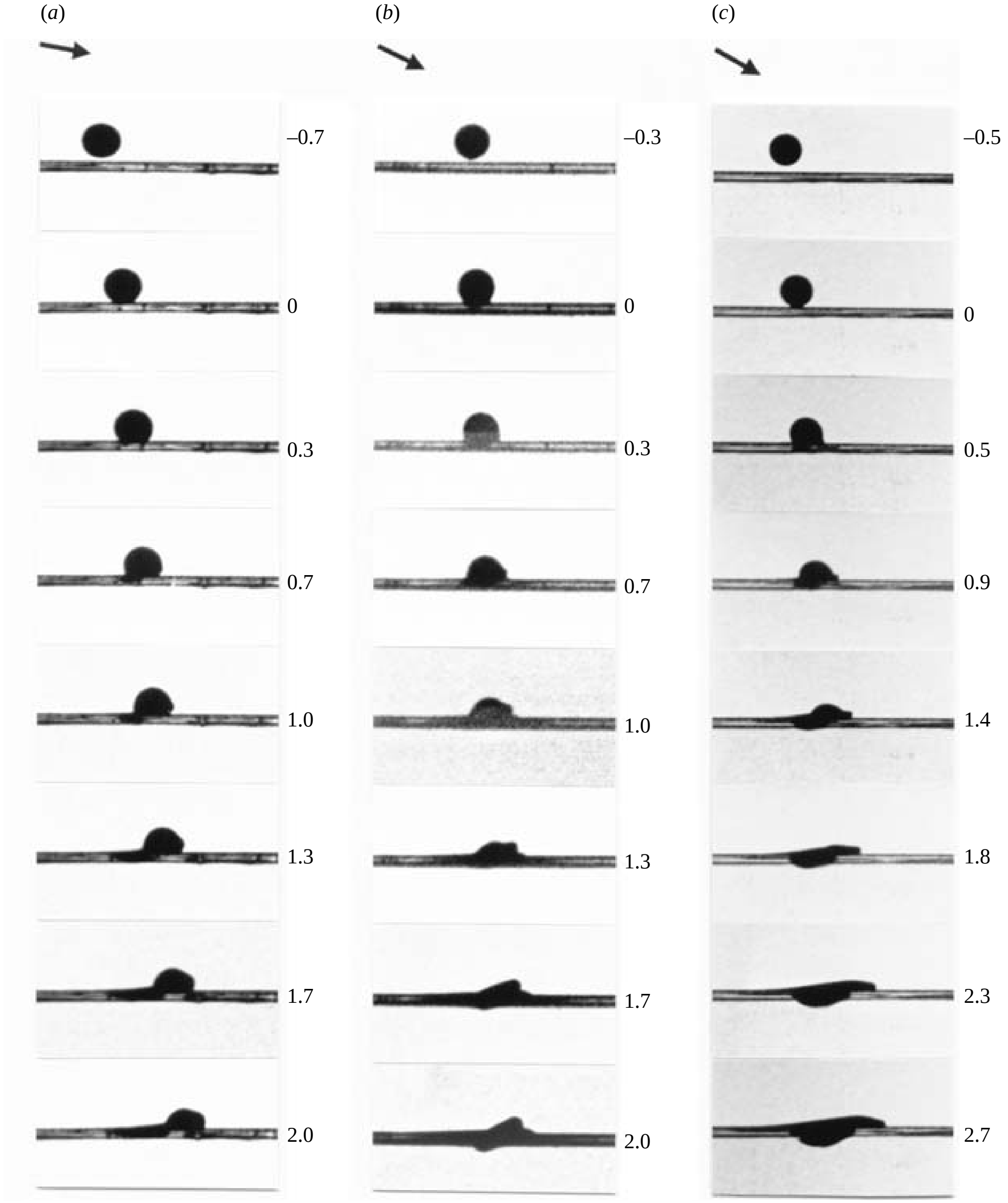

FIGURE 2. First stages of coalescing drop impact in lateral perspective, numbers on the photographs refer to the dimensionless time τ with respect to the moment of first contact. Arrows on top of the columns indicate the direction and angle of impact. (*a*) Impact parameters: $\alpha = 10.8^\circ$; $D = 1.9\,\mathrm{mm}$; $u_i = 1.51\,\mathrm{m\,s^{-1}}$; $We = 75.7$; $We_N = 2.7$; $Re = 287$; $Fr = 122$. (*b*) Impact parameters: $\alpha = 26.6^\circ$; $D = 1.55\,\mathrm{mm}$; $u_i = 1.23\,\mathrm{m\,s^{-1}}$; $We = 41.0$; $We_N = 8.2$; $Re = 191$; $Fr = 100$. (*c*) Impact parameters: $\alpha = 29.2^\circ$; $D = 2.0\,\mathrm{mm}$; $u_i = 2.15\,\mathrm{m\,s^{-1}}$; $We = 162$; $We_N = 38.4$; $Re = 430$; $Fr = 236$.

3. Results

3.1. *First stage of impact in lateral perspective*

Figure 2 shows visualizations of the first stage of impact in lateral perspective at eight different steps of the dimensionless time τ with respect to the moment of first contact. Two optical problems have to be taken into account for the interpretation of the visualizations: First, it is impossible to distinguish between zones where the illuminating light is refracted due to inclined air/water interfaces and those where it is extinguished by the dye in the drop fluid. Refraction results in completely dark zones due to the shadowgraph optics employed, as can be seen in figure 1(*b*). Extinction by dye only produces zones of complete darkness where the dye layer is thick (minimum layer for complete extinction approximately 0.5 mm); in thin layers, extinction is proportional to the layer thickness. Thus, the distribution of drop fluid can only be recognized without ambiguity when surface perturbations have disappeared sufficiently. Secondly, the two horizontal lines in the visualizations in lateral perspective are the rims of the front and back wall of the glass cuvette containing the target fluid. Owing to optical parallax they appear as two distinct lines, the upper line represents the front wall. This means that on all visualizations in lateral perspective the air/water interface of the unperturbed target fluid is seen from below at an angle of 0.74°.

Figure 2(*a*) depicts an impact at low normal Weber number $We_N = 2.7$ and $\alpha = 10.8^\circ$. In this case, a sharp kink appears in the front part of the drop contour at $\tau \geqslant 0.7$, which propagates upwards to the zenith of the drop. We interpret this kink to be a convex capillary wave. Only a few impact visualizations show in addition a kink in the rear part of the drop contour. The term ‘convex’ is used in the sense that the centre of the surface curvature is in the drop fluid. Figure 2(*b*) shows an impact at $We_N = 8.2$ and $\alpha = 26.6^\circ$ where a capillary wave is not only visible on the front part of the drop contour (beginning at $\tau = 0.7$), but also on the target fluid (beginning at $\tau = 1.0$). Both waves propagate away from the contact line as can be seen when the visualizations for $0.7 \leqslant \tau \leqslant 2.0$ are compared. In figure 2(*c*), impact at $We_N = 38.4$ and $\alpha = 29.2^\circ$ is shown, where a step-like contour develops in the front part of the drop at $\tau = 0.9$. We interpret this step-like contour as a lamella, which is ejected at the contact line of both fluids. Further experimental evidence for our interpretations is given in §§ 3.3 and 3.4, numerical results on lamella formation and the contributions of drop and target fluid are presented in § 3.8, and in § 4 possible physical mechanisms for the described phenomena are discussed.

In figure 3, the regimes for capillary wave formation (open squares) or lamella ejection (filled rhombuses) are shown in the (We_N, α)-plane. Impacts that could not be classified without ambiguity are indicated as ‘transitional’ (open triangles). As can be seen in figure 3, there is an abrupt threshold at $We_N = 10$ between the two impact outcomes which shows no dependence on the impact angle α. The fact that the threshold between the two regimes depends solely on the normal Weber number indicates that the normal component of the impact velocity $u_{i,N}$ and not the absolute magnitude of u_i is the decisive parameter.

3.2. *Fluid–fluid interface and partial immersion of drop fluid*

Figure 4 shows the spreading of drop fluid onto the target surface. In the case of glancing impact, shown in figure 4(*a*) for $\alpha = 6.3^\circ$ and $We = 70.8$, the drop forms a plane layer on the target fluid surface without any visible immersion of drop fluid into the target fluid.

In figures 4(*b, c*), partial immersions can be seen. Since figure 4(*b*) shows two different types of immersion we will first discuss figure 4(*c*). In figure 4(*c*), the drop hits the target fluid surface with an impact angle $\alpha = 57.5^\circ$ and $We = 37.6$ forming a deep crater. At $\tau = 2.1$, a cusp appears at the crater rear. At later stages ($\tau \geqslant 3.0$), the cusp propagates towards the bottom of the crater which itself is stationary with

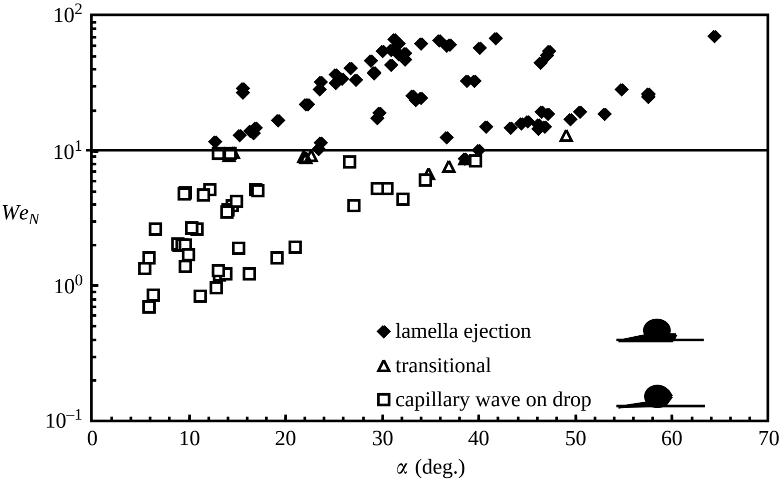

FIGURE 3. Regimes for capillary wave formation on drop or lamella ejection in the (We_N, α)-plane. Impacts that could not be classified without ambiguity are indicated as ‘transitional’.

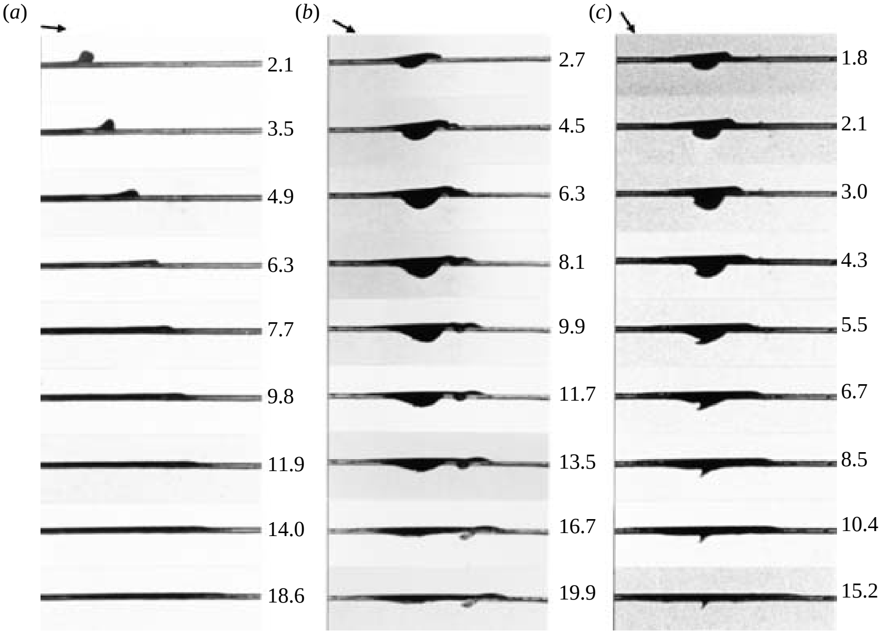

FIGURE 4. Fluid–fluid interface and partial immersion of drop fluid. (*a*) Drop fluid spread evenly on target fluid surface, $\alpha = 6.3°$; $D = 1.8\,\mathrm{mm}$; $u_i = 1.50\,\mathrm{m\,s^{-1}}$; $We = 70.8$; $We_N = 0.9$; $Re = 270$; $Fr = 127$. (*b*) Partial immersion at the front of the spreading drop; $\alpha = 29.2°$; $D = 2.0\,\mathrm{mm}$; $u_i = 2.15\,\mathrm{m\,s^{-1}}$; $We = 162$; $We_N = 38.4$; $Re = 430$; $Fr = 236$. (*c*) Partial immersion of drop fluid into the target fluid at the crater rear; $\alpha = 57.5°$; $D = 1.6\,\mathrm{mm}$; $u_i = 1.16\,\mathrm{m\,s^{-1}}$; $We = 37.6$; $We_N = 26.8$; $Re = 186$; $Fr = 85.7$.

respect to the target fluid once it has reached its greatest extent. When the crater has almost disappeared at $\tau = 15.2$ the cusp prevails, it therefore represents drop fluid which is immersed into the target fluid, although we cannot say precisely when the immersion of drop fluid starts.

In figure 4(*b*), drop impact at $\alpha = 29.2°$ and $We = 162$ is shown. In addition to the immersion at the rear part of the crater, a second partial immersion occurs in the front part of the spreading drop. Beginning at $\tau > 2.7$, a second step occurs in the lateral view of the front contour of the drop; it can be seen clearly at $\tau = 4.5$. At $\tau \geqslant 8.1$, a partial immersion of drop fluid into the target fluid can be detected, which further develops and forms a bent loop at the end of the visualization series at $\tau = 19.9$. The immersion appears as if the drop fluid becomes involved in a vortex; this will be discussed in § 4.

To avoid misinterpretations of figure 4(*b*), we would like to point out that the bright line below the drop front (and between the rims of the cuvette) is produced by the optical parallax discussed above. A bright line below the spreading drop can also be seen in figure 4(*a*) where the drop spreads smoothly on the target surface.

Figure 5 depicts the regimes of partial immersion of drop fluid into the target fluid volume. Figure 5(*a*) shows the regimes in the (α, We)-plane of the cusp-shaped immersion at the rear part of the crater, as shown in figure 4(*c*). As can be seen in figure 5(*a*), no immersion can be visualized for $\alpha < 23°$ (filled squares), whereas for $\alpha > 23°$ this type of partial immersion always occurs (open squares). However, it has to be added that the classification 'no immersion' only means that an immersion could not be visualized, which might be a problem of the opacity at the target surface. Therefore, only the confirmation of an existing immersion is unambiguous in a rigorous sense. This technical restriction also applies to figure 5(*b*).

In figure 5(*b*), the regimes of the immersions in the front part of the spreading drop are shown in the (We, α)-plane. It must be pointed out that there are apparently two types of immersion in the front range of the spreading drop, the one which was observed more frequently being shown in figure 4(*b*), the other in figure 8(*b*). It seems that the front immersion type shown in figure 4(*b*) (open squares) depends on We_N as it only occurs for $We_N > 10$, this threshold being drawn as a dashed curve in figure 5(*b*). However, for $We < 50$, no such immersion becomes visible, even for $We_N > 10$, so that this condition is necessary, but not sufficient for the occurrence of an immersion in the front range of the spreading drop. The second front immersion type shown in figure 8(*b*) also occurs for $We_N < 10$ (open triangles). There are two cases to which this description applies in figure 5(*b*) which may be characterized by the fact that their Weber number was rather high, i.e. $We > 140$. A comparison of lateral and vertical views regarding partial immersion behind the drop front will be given in § 3.6. Possible mechanisms for the generation of partial immersions of drop fluid into the target fluid will be discussed in § 4.

Summarizing the results concerning partial immersions of drop fluid, it may be said that for $We_N < 10$, $We < 140$ and $\alpha < 23°$ impinging drops spread out evenly with no visible immersion so that drop impact ends with a plane layer of drop fluid spread on the target fluid. For $\alpha > 23°$, drop fluid is immersed in the rear part of the spreading drop. For the two types of front immersion, the two conditions:

(i) $We_N > 10$ and $We > 50$, immersion type shown in figure 4(*b*),
(ii) $We > 140$ and $\alpha < 23°$, immersion type shown in figure 8(*b*),

could be found. For some impacts even two or three loop-formed immersions in the front part, as shown in figure 4(*b*), develop in series (open rhombuses in figure 5*b*).

3.3. *Vertical perspective: spreading velocity*

Figure 6(*a*) shows the evolution of drop spreading in vertical perspective for $\alpha = 19.9°$, $We = 165$. For comparison, another impact recorded in lateral perspective is shown in figure 6(*b*) for $\alpha = 19.2°$, $We = 155$. In figure 6(*a*), seven time steps out of a series

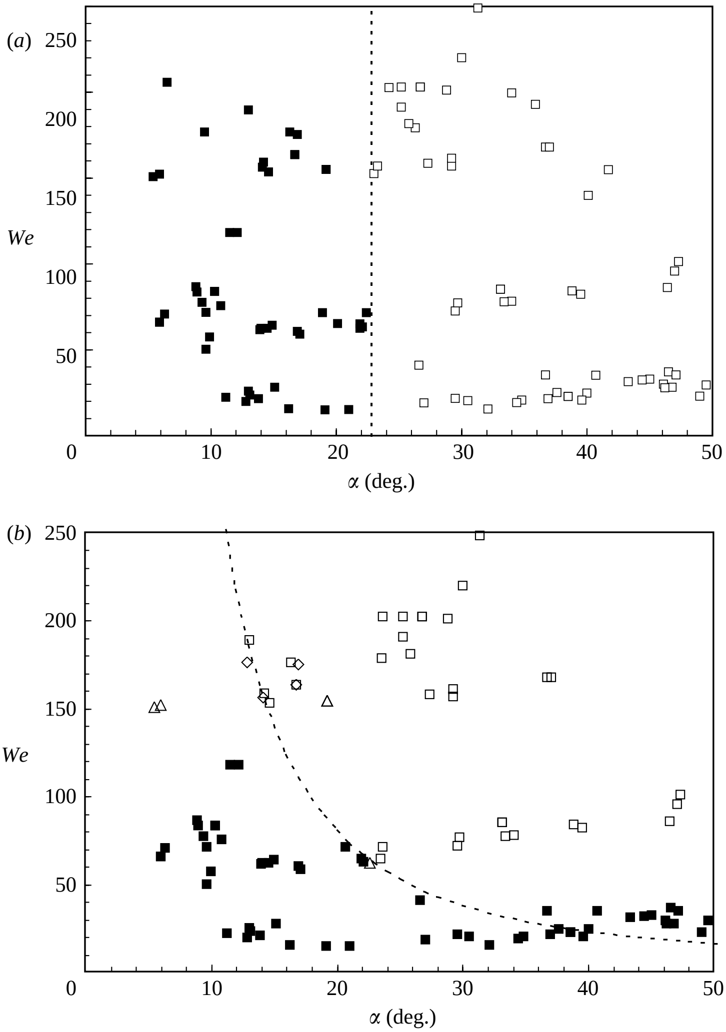

FIGURE 5. Regimes of partial immersion of drop fluid into the target fluid volume in the (We, α)-plane. (*a*) Cusp-formed immersion at the crater rear. ■, no immersion; □, immersion as shown in figure 4(*c*). (*b*) Immersion behind the front of the drop. ■, no immersion; □, immersion as shown in figure 4(*b*); △, immersion as shown in figure 8(*b*); ◇, two immersions, one as shown in figure 4(*b*) and one as shown in figure 8(*b*).

of 60 pictures are shown (time interval between flashes: 0.94 ms). The first image shows the oscillating drop just before coalescence in its oblate phase at $\tau = -0.2$. The second image at $\tau = 0.8$ is the first after impact, where the deformation of the target fluid surface refracts the flashlight so that dark areas are either dyed drop volume or waves on the target fluid; the same applies to the images at $\tau = 4.0$, 15.7 and 21.0. At $\tau = 31.6$ and 63.4, the front wave is far detached from the drop fluid so that the pattern formed by the dyed drop volume can be recognized clearly. The terms ‘front wave’ and ‘left and right crater waves’ are explained in figure 6(*a*). Recording of the impact shown in figure 6(*b*) with $\alpha = 19.2°$ and $We = 155$ ends at $\tau = 20.7$. Therefore, no comparison is possible for $\tau = 31.6$ and 63.4.

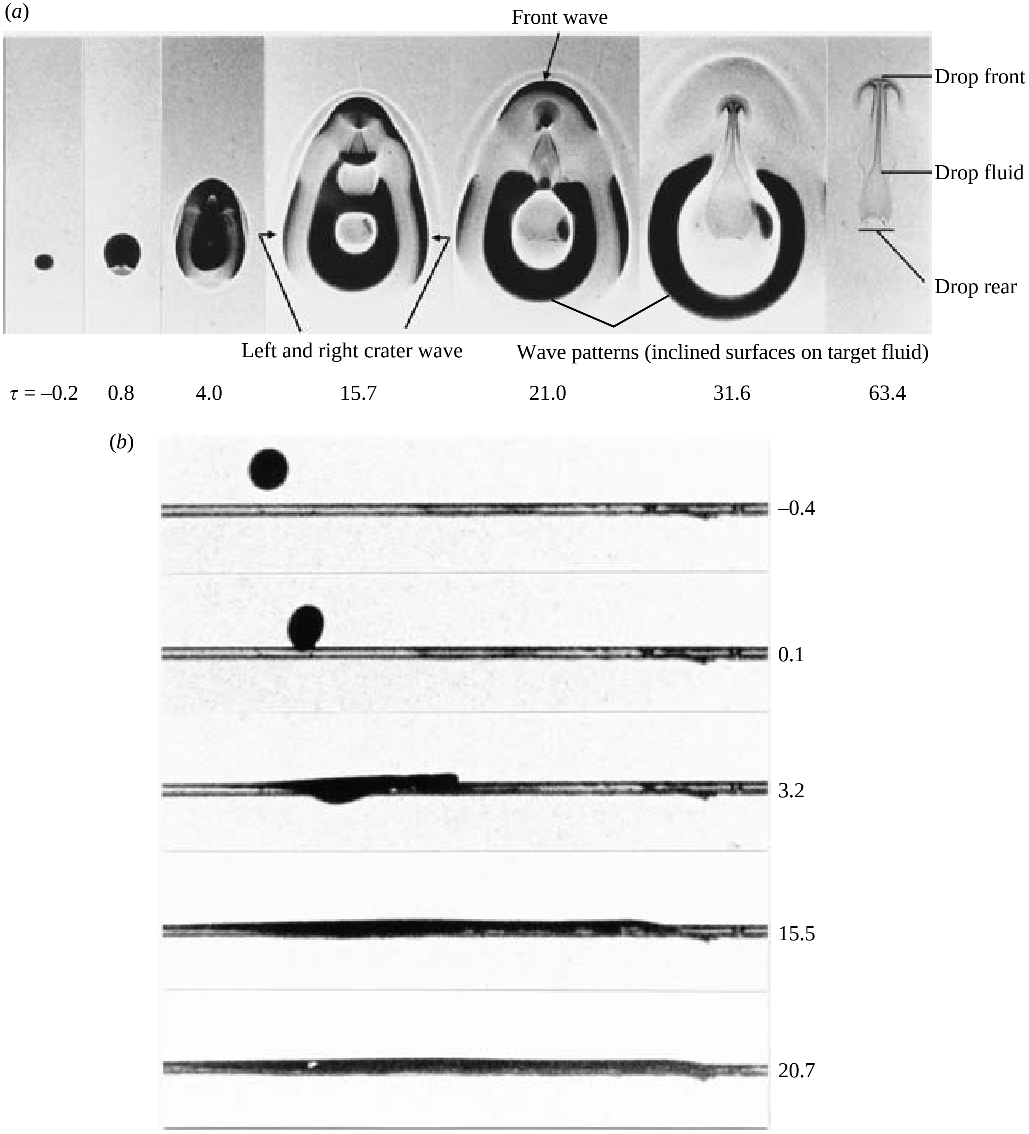

FIGURE 6. Evolution of drop spreading at different time stages. (*a*) Vertical perspective for $\alpha = 19.9^\circ$; $D = 1.95\,\mathrm{mm}$; $u_i = 2.20\,\mathrm{m\,s^{-1}}$; $We = 165$; $We_N = 19.1$; $Re = 429$; $Fr = 253$. (*b*) Lateral perspective for $\alpha = 19.2^\circ$; $D = 1.8\,\mathrm{mm}$; $u_i = 2.22\,\mathrm{m\,s^{-1}}$; $We = 155$; $We_N = 16.8$; $Re = 400$; $Fr = 279$.

The evolution of drop spreading and velocities of wave propagation were determined from the visualizations of figures 6(*a*) and 6(*b*) and are shown in figures 7(*a*) and 7(*b*). As can be seen, vertical (filled squares) and lateral recording (open squares) match very well, taking into account that impact conditions are only similar, but not identical. In figure 7(*a*), the front wave and the drop front are apparently at the same height until $\tau \approx 16$ where the extrapolation of the front of the spread drop intersects the curve of the front wave. For $\tau \geqslant 16$, the spread drop volume has almost come to rest on the target fluid, its slow movement in the forward direction results presumably

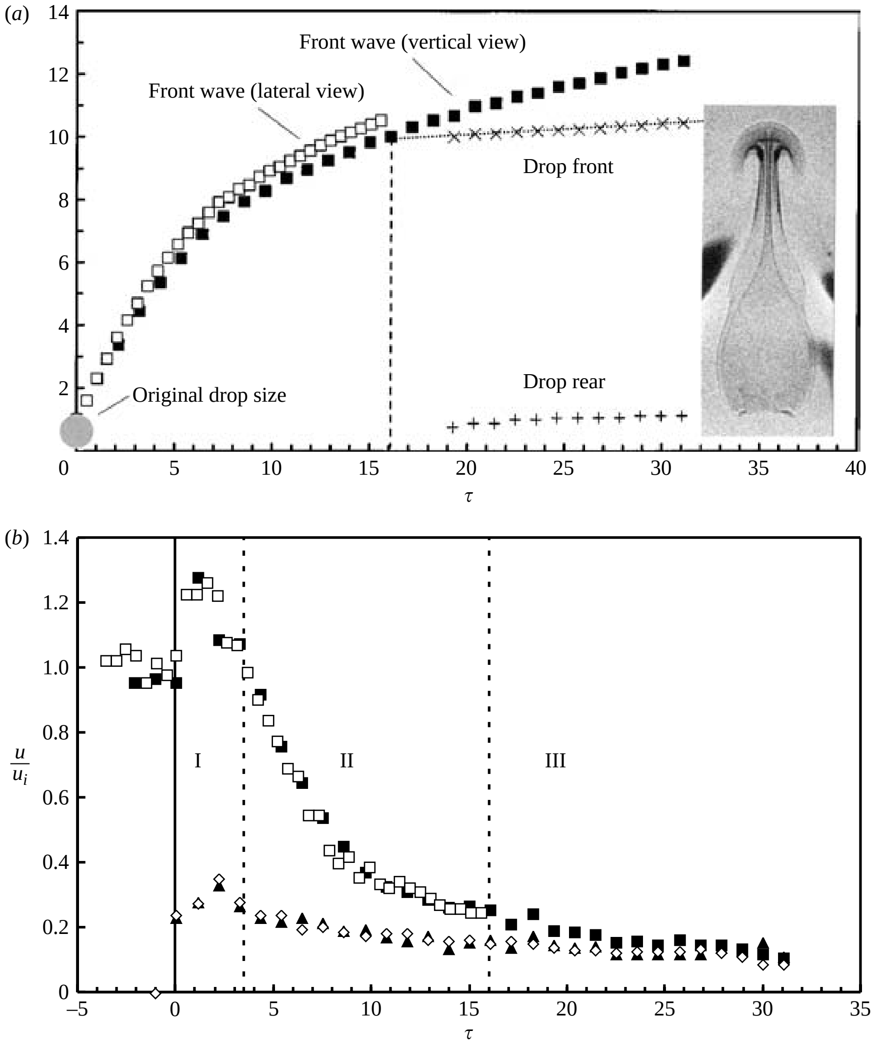

FIGURE 7. (*a*) Spreading of drop volume on the target fluid *vs.* time. Two impact events are compared. Vertical view: impact parameters given in the caption to figure 6(*a*); lateral view: impact parameters given in the caption to figure 6(*b*). (*b*) Velocity evolution during drop spreading, data of figure 7(*a*) differentiated. □, velocity of front wave of figure 6(*a*); ■, velocity of front wave of figure 6(*b*); □, left crater wave; ◇, right crater wave. Three stages I, II and III can be classified during impact, see text.

from the velocity field that the drop induced on the target fluid during impact. Thus, it may be assumed that the front wave detaches at $\tau \approx 16$ from the drop front.

Figure 7(*b*) shows the velocity evolution of waves on the target fluid, generated by differentiation of the data shown in figure 7(*a*). The velocity of the front wave is shown as filled (vertical view) and open squares (lateral view). It can be seen that there are three stages (I, II, III) of the velocity u_{fw} of the front wave: During stage I, the front wave (together with the drop front, see above) propagates with a velocity which is at most 20% larger than u_i. For $\tau \geqslant 3$, u_{fw} becomes smaller than u_i, indicating the beginning of stage II where u_{fw} decreases approximately exponentially. This means that the drop, the driving force of the front wave, loses kinetic energy owing to its interaction with the target fluid. For $\tau \geqslant 16$, which indicates the beginning of stage III, u_{fw} becomes equal to the velocity of the crater waves propagating in the lateral direction (filled triangle: left crater wave; open rhombuses: right crater wave) with their slow decrease in wave velocity with time. From figure 7(*b*), it has to be concluded that the drop fluid no longer moves relative to the target surface for $\tau \geqslant 16$. Thus, the result found by differentiation shown in figure 7(*b*) agrees with that found via extrapolation of the drop front in figure 7(*a*).

It may be pointed out that the pattern of the spread drop in figure 7(*a*) is surrounded by an outer sharp line of drop fluid. We interpret this outer surrounding line as a result of the lamella produced in the first stage of impact for $We_N > 10$, see § 3.1. This phenomenon will be discussed in detail in § 3.4.

In figures 8 and 9, impact at low normal Weber number, i.e. $We_N < 10$ will be shown. Figure 8(*a*) depicts visualizations at glancing α with $\alpha = 7.4°$ and $We = 158$ in vertical perspective, figure 8(*b*) in lateral perspective with $\alpha = 5.9°$ and $We = 152$. Figure 9 represents the velocity evolution of the wavefronts of figure 8(*a*, *b*). We will first focus our attention on the velocity evolution; morphological features will be described in §§ 3.4 and 3.5. As can be seen in figure 9, the velocity of the front of the flying drop before impact ($\tau < 0$) undulates owing to drop contour oscillations (prolate/oblate). Open squares refer to the vertical view shown in figure 8(*a*), filled squares to the vertical view shown in figure 8(*b*). As in figure 7, the evolution of the front wave velocity u_{fw} can be classified into three stages, but in this case, u_{fw} does not exceed the impact velocity u_i. Instead, u_{fw} decreases roughly linearly in stage I. At $\tau \approx 8$, the decrease of u_{fw} changes abruptly, indicating the beginning of stage II with an approximately exponential decrease of u_{fw}. Stage III is reached at $\tau \approx 17$. It may be noted that the two impacts being compared (figure 8*a*, *b*) not only differ slightly in their impact parameters, but are also shifted in their phase of drop contour oscillation at the moment of impact. Because of this, we suppose that the transition from stages I to II, i.e. the transition from a linear to an approximately exponential decrease in u_{fw}, differs in the comparison of vertical and lateral recordings shown in figure 9 ($\tau \approx 6.9$ for figure 8*a* and $\tau \approx 8.7$ for figure 8*b*).

The main difference between figures 7(*b*) and 9 is that u_{fw} exceeds u_i by as much as 28% (figure 7 *b*) whereas in figure 9, u_{fw} never exceeds u_i. This finding can even be generalized for all of our experiments: in all drop impacts with $We_N < 10$, u_{fw} was never found to exceed u_i, whereas in those with $We_N > 10$, u_{fw} always exceeds u_i during stage I (result scrutinized for 11 impact events). These findings can be interpreted such that in all impacts with $We_N > 10$, the lamella ejected at the contact line of drop and target fluid raises u_{fw}, whereas in those cases with $We_N < 10$, the capillary wave has no effect on u_{fw}. In all impacts investigated in detail, we found u_{fw} to exceed u_i at its maximum by a factor of 1.1 ($We_N = 10.7$) to 1.6 ($We_N = 62.9$). The maximum of u_{fw} appeared to be proportional to We_N, but unfortunately the temporal resolution of the recordings (0.42 ms and 0.94 ms for lateral and vertical perspective, respectively) did not allow a more precise estimate of u_{fw}.

The fact that u_{fw} decreases approximately linearly in stage I and exponentially in stage II in the impacts shown in figures 8(*a*) and 8(*b*) could be interpreted in the following manner: after first contact, the drop is decelerated at the contact interface and therefore gains angular momentum, resulting in a vortical motion inside the drop over the target surface. Because of viscosity, the drop leaves a trace of dyed drop fluid behind. At $\tau \approx 8$, the drop volume has decreased to an extent that a transition from the vortical motion to sliding takes place, which means that the remaining drop fluid drags the uppermost layer of the target fluid with the drop and generates a boundary

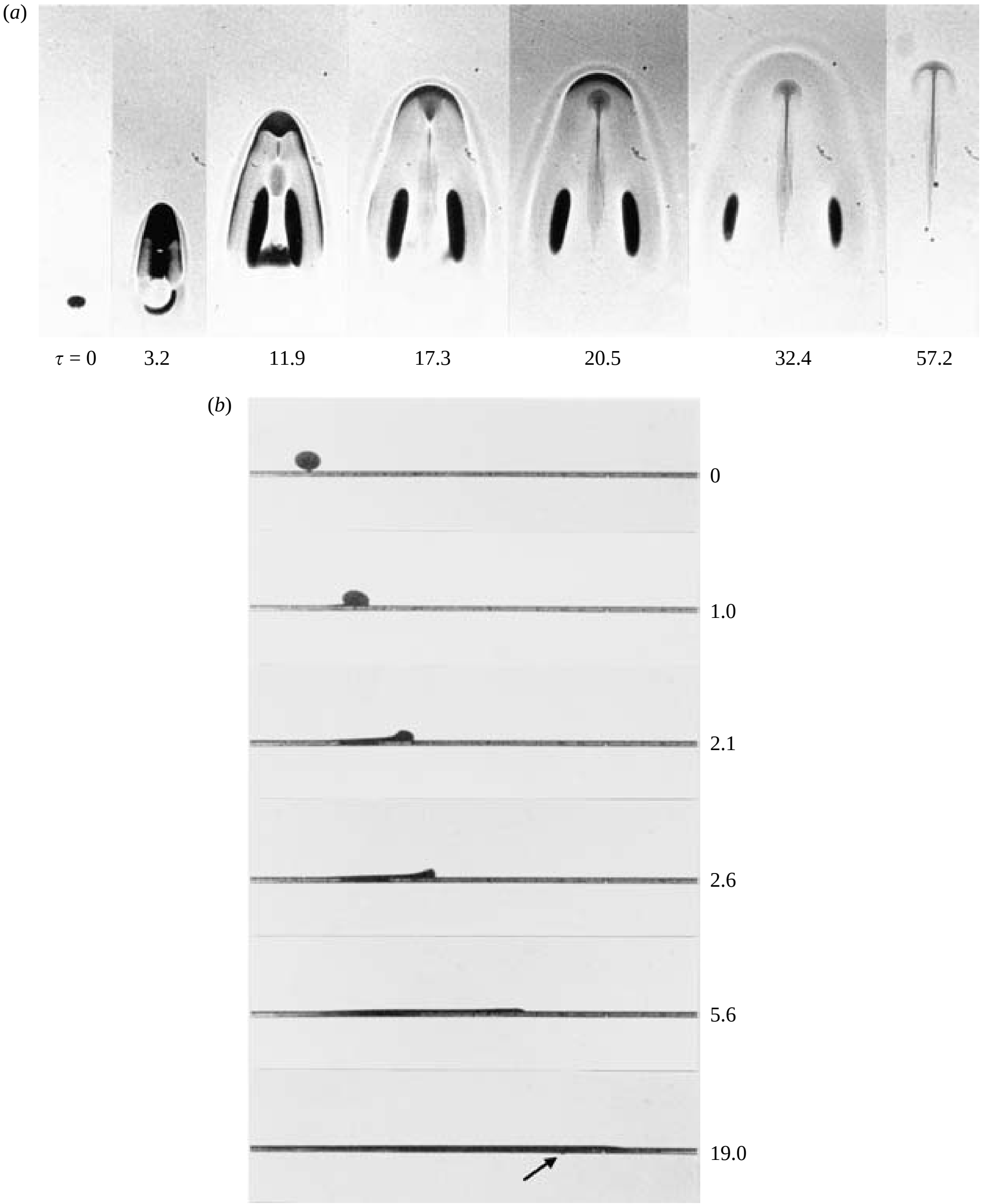

FIGURE 8. Evolution of drop spreading at different time stages. (*a*) Vertical perspective for $\alpha = 7.4^\circ$; $D = 1.9\,\mathrm{mm}$; $u_i = 2.18\,\mathrm{m\,s^{-1}}$; $We = 158$; $We_N = 2.6$; $Re = 414$; $Fr = 255$. (*b*) Lateral perspective for $\alpha = 5.9^\circ$; $D = 1.8\,\mathrm{mm}$; $u_i = 2.20\,\mathrm{m\,s^{-1}}$; $We = 152$; $We_N = 1.6$; $Re = 396$; $Fr = 274$.

layer in the target fluid. When the drop slides on the target fluid surface, it quickly loses momentum and comes to rest. Sliding produces lateral thinning of the trace of drop fluid left on the target surface with a circular volume of drop fluid remaining compact at the front, as can be seen when the drop has come to rest (see figure 8*a*, $\tau = 20.5$). Of course, the interpretation given here would need detailed experimental and numerical verification.

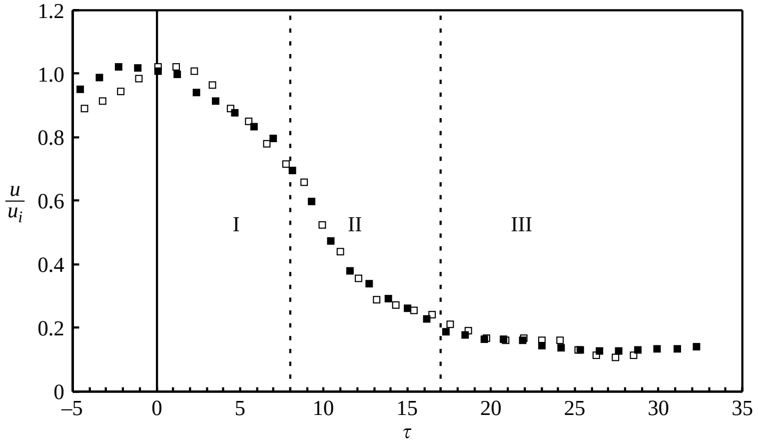

FIGURE 9. Velocity evolution during drop spreading. □, vertical view, impact parameters given in figure 8(*a*); ■, lateral view, impact parameters given in figure 8(*b*). Three stages I, II and III can be classified during impact, see text.

3.4. *Vertical perspective: morphology of spread drops*

In figure 10, the diverse patterns of spread drops are shown in the (α, *We*)-plane. The most striking observation to be made is that changes in pattern morphology are mostly not continuous, but occur in discrete steps so that the different patterns can be classified into several groups of similar patterns. For the parameter range covered in this study, we found ten different patterns of spread drops; their impact parameters (α, *We*) are shown in figure 10(*a*) and the visualizations of the drop fluid patterns are displayed in figure 10(*b*). The different patterns are termed (i)–(x); all parameters of the visualizations shown in figure 10(*b*) are summarized in table 2. The four impacts with drop pattern (vii) are compared in figure 10(*c*) with their final images at $\tau = 46.2 \pm 0.1$ to give an impression of the reproducibility of patterns of the same class, but different impact parameters (*We*, α). The respective impact parameters are given in table 2.

It must be taken into account when comparing the different visualizations in figure 10(*b*) that the last image of each recording was always taken so that the drop has come to rest on the target fluid, but τ is different in each case (see table 2). In the case of pattern (iii), recording ceases before the drop has come to rest; in that of pattern (x), the pattern has presumably come to rest, but not the crater wave. We will first describe general aspects of the classification and then focus the description on the particular features of the drop morphologies.

The threshold $We_N = 10$ is inserted as a curved line in figure 10, since $We = We_N \sin^{-2}\alpha$. All other lines are arbitrarily drawn straight, just to discriminate roughly the parameter regions where different patterns are found. The arbitrariness comes from the fact that there are too few data points to estimate the shape of the boundaries between the regimes more precisely. Comparing the patterns with $We_N < 10$ to those with $We_N > 10$ in figure 10(*b*), we can see that all patterns with $We_N > 10$ (i.e. (iv)–(x)) are surrounded by an outer sharp line of drop fluid (in the case of pattern (vi), the surrounding line can only be seen in the rear part). No patterns with $We_N < 10$ (i.e. (i)–(iii)) possess such a surrounding line. We interpret the outer surrounding line of the spreading patterns as a result of the lamella being ejected in all impacts with

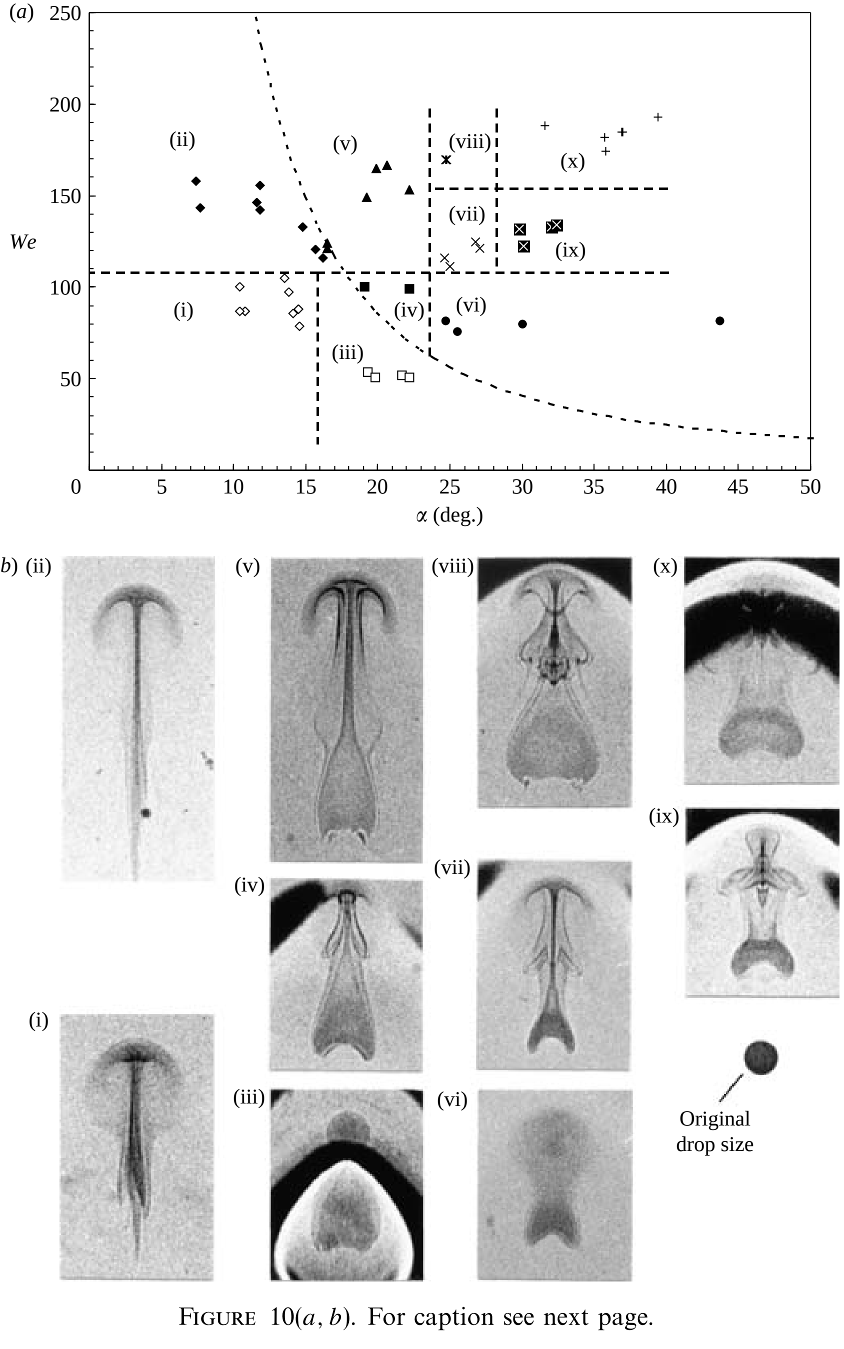

FIGURE 10(a, b). For caption see next page.

$We_N > 10$, as is shown in lateral perspective in § 3.2 and its spreading velocity being analysed in § 3.3.

Despite the limited accuracy of the boundaries between the different regimes in figure 10, the transition taking place at $\alpha \approx 23^\circ$ corresponds quite well with the findings in lateral perspective, i.e. figure 5. Figure 5(a) summarizes the fact that, for $\alpha > 23^\circ$, a partial immersion of drop fluid in the rear part of the spreading pattern becomes visible. We can see in figure 10(b) that the rear part of the patterns (vi)—(x)

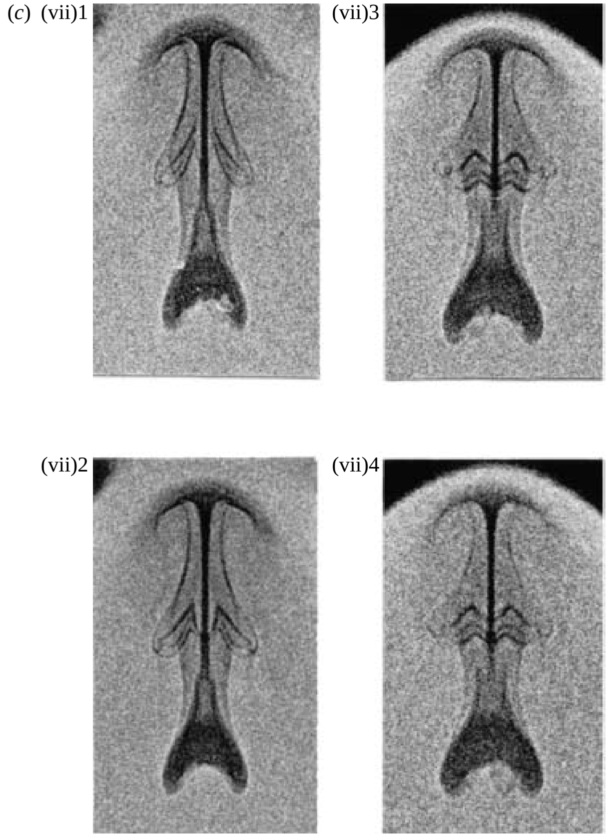

FIGURE 10. Morphology of spread drops at rest after impact. (*a*) Classification into groups of similar spreading patterns in the (α, *We*)-plane. Curved line: $We_N = 10$. (*b*) Visualizations of different spreading patterns, impact parameters: see table 2. (*c*) Final images of the four impacts with pattern (vii), impact parameters: see table 2.

has a much higher dye intensity than most other parts of the same pattern. This does not apply to $\alpha < 23°$, i.e. patterns (i)–(v), where the rear part of the spreading pattern has no greater dye intensity than most other parts of the same pattern. We can assume that the high dye intensity in the rear part of patterns (vi)–(x) results from the drop fluid being immersed in the target fluid, see also § 3.6.

Morphologically, the rear part in the patterns (vi)–(x) has the form of a fish fin or kidney, and it is wider than the succeeding middle part of the same pattern. The maximum width of the rear part of patterns (vi)–(x) is found in the interval between $1.6D$ and $3.5D$, which indicates that broadening of the drop takes place at initial contact when the rear part of the spreading pattern is formed. However, since the time τ differs for the spreading patterns shown in figure 10(*b*), these values only illustrate the range which was found.

We will now discuss the front of the spreading patterns. It can be seen in figure 10(*b*) that the patterns (i), (ii), (v), (vii), (viii) and (x) have a front formed like an anchor, while for patterns (iii), (iv), (vi) and (ix), the front fluid is compact and approximately circular. When comparing the evolution of the spreading patterns in figures 6 and 8, we can see that the drop front is formed as a disk of roughly circular shape followed by a thin neck once the drop fluid has come to rest on the target

Pattern type	α (deg.)	D (mm)	u_i (m s^{-1})	We	We_N	Re	Fr	τ
Figure 10(b)								
(i)	10.8	1.80	1.66	87	3.0	299	156	44.2
(ii)	7.4	1.90	2.18	158	2.6	414	255	60.4
(iii)	19.3	1.70	1.34	53	5.8	228	108	15.6
(iv)	19.1	1.85	1.76	100	10.7	326	171	33.1
(v)	19.9	1.95	2.20	165	19.1	429	253	63.4
(vi)	24.7	1.90	1.57	82	14.3	298	132	35.7
(vii)	25.0	1.90	1.83	111	19.9	348	180	47.1
(viii)	24.7	1.95	2.23	169	29.6	435	260	?*
(ix)	32.0	1.90	2.00	133	37.3	380	215	49.5
(x)	35.7	1.90	2.34	182	61.9	445	294	67.1
Figure 10(c)								
(vii) 1	24.6	1.9	1.87	116	20.1	355	188	46.3
(vii) 2	25.0	1.9	1.83	111	19.9	348	180	46.2
(vii) 3	26.8	1.9	1.94	125	25.4	369	202	46.1
(vii) 4	27.1	1.9	1.91	121	25.1	363	196	46.3

TABLE 2. Parameters of the visualizations shown in figure 10(b, c).
*Beginning of drop impact not recorded.

fluid. This stage can be seen in figure 6(a) at $\tau = 21.0$ and in figure 8(a) at $\tau = 17.3$ and 20.5. Owing only to the velocity field on the surface of the target fluid, which has been induced by the impact, the drop fluid slowly deforms. In figure 6(a), $\tau = 31.6$ and 63.4 and in figure 8(a), $\tau = 32.4$ and 57.2, it can be seen how the anchor form of the front develops.

Two conclusions may be drawn from figures 6(a) and 8(a) and the overview in figure 10(b). First, the front pattern is not produced directly by the momentum of the impacting drop, but rather by the induced velocity field on the surface of the target fluid, because it develops only when there is no more relative movement of drop fluid on the target surface. Secondly, a minimum of the tangential component of the impact velocity $u_{i,T}$ is obviously required to induce a velocity field on the target surface. For $u_{i,T}$ that is too low, capillary forces are presumably higher than convective forces and lead to an approximately circular shape of the front part of the spreading drop as in the case of pattern (vi). When figure 10(b) is displayed using the Weber number We_T formed with the tangential velocity component $u_{i,T}$, the change between the roughly circular drop front and the one of anchor character occurs at $We_T \approx 90$, but it is dependent on α, slightly increasing with growing α. It may be speculated that the transition from the circular drop front type to the anchor type is continuous and not at a precise threshold.

3.5. *Vertical perspective: induced velocity field on target surface*

As pointed out in the previous paragraph, the impacting drop induces a velocity field in the target fluid, which becomes visible on its surface when the drop fluid no longer moves relative to the surface, i.e. when the front wave detaches from the drop front. Figure 11 shows the deformation of the spread drop fluid; the two patterns are taken from the impact shown in figure 8(a), $\tau = 20.5$ (grey area) and 57.2 (area inside the solid black line). Owing to this velocity field, the front part of the spread drop fluid is expanded to an anchor-like pattern, whereas the rear part is compressed. To characterize the (unsteady) velocity field qualitatively, estimated streamlines are drawn

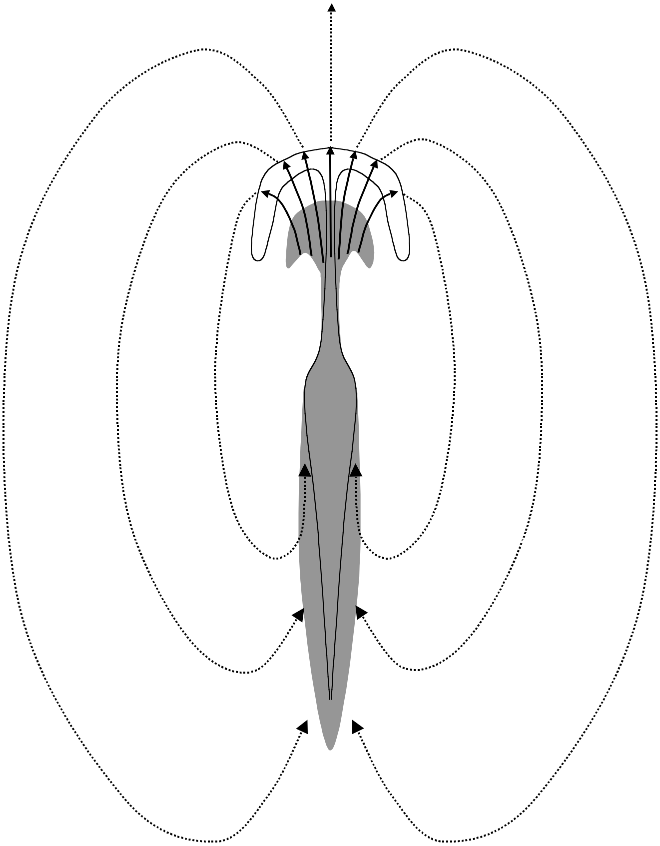

FIGURE 11. Sketch of induced velocity field on target fluid surface. The spreading pattern of drop impact shown in figure 8(*a*) is shown for $\tau = 20.5$ (grey area) and $\tau = 57.2$ (area inside the solid black line). The velocity field is drawn tentatively with arrows to give a qualitative impression.

by hand in figure 11. The fact to be illustrated by figure 11 is that the anchor-like front part of most spreading patterns, especially patterns (i), (ii), (v), (vii), (viii) and (x) in figure 10, is not produced as long as drop fluid moves relative to the target fluid (stage II in figures 7(*b*) and 9), but only once the drop has come to rest relative to the target surface (stage III in figures 7(*b*) and 9). This can also be seen on the visualizations in figure 6(*a*), comparing $\tau =$ 21.0 and 63.4.

Also, the central indentation in the rear part which can be seen in most pattern types ((iii)–(x)) in figure 10 is produced by the induced velocity field. This statement can be proved by studying the time evolution of drop spreading: as can be seen in figure 6 (*a*), the outline in the rear part is straight at $\tau = 31.6$, but curved at $\tau = 63.4$. Thus, the rear part in all patterns (iii)–(x) is modified under the action of the induced velocity field that deforms the initial pattern produced by the momentum of impact to yield its final fin-like form.

3.6. *Correspondence of phenomena observed in vertical and lateral perspective*

Two sets of impacts in vertical and lateral perspective will be discussed, one quantitatively for $We \approx 80$, $\alpha \approx 30°$, the other qualitatively for $We \approx 150$, $\alpha \approx 30°$. The evolution of drop spreading is displayed in a quantitative diagram of drop position *vs.* time in figure 12 for two similar impact events in vertical ($\alpha = 30.0°$; $We = 79.7$) and

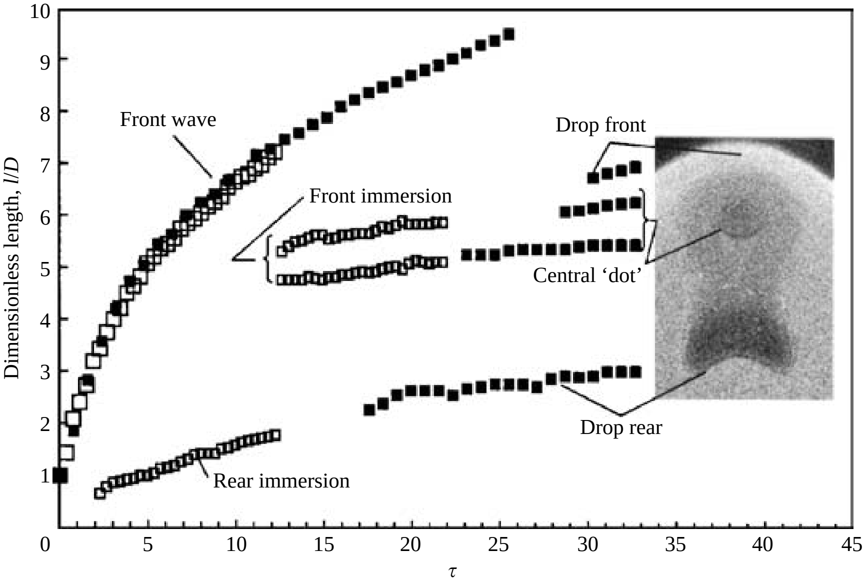

FIGURE 12. Temporal evolution of drop spreading: comparison of □, lateral and ■, vertical perspective. Vertical perspective: $\alpha = 30.0°$; $D = 1.85\,\text{mm}$; $u_i = 1.57\,\text{m s}^{-1}$; $We = 79.7$; $We_N = 19.9$; $Re = 290$; $Fr = 136$. Lateral perspective: $\alpha = 29.7°$; $D = 1.75\,\text{mm}$; $u_i = 1.59\,\text{m s}^{-1}$; $We = 77.3$; $We_N = 18.0$; $Re = 278$; $Fr = 147$.

lateral perspective ($\alpha = 29.7°$; $We = 77.3$). Unfortunately, recording of the impact in lateral perspective ceases at $\tau = 21.8$ when the contours of the spread drop in vertical view cannot yet be recognized owing to surface waves. Therefore, the correspondence of the partial immersions in lateral perspective to morphological structures in vertical view can only be assessed via extrapolation. As can be seen in figure 12, the rear immersion in lateral perspective matches reasonably well with the drop rear seen in vertical perspective when a linear extrapolation is applied. The same accounts for the front immersion visualized in lateral perspective that corresponds to a central 'dot' of higher dye intensity in the front part of the spread drop in vertical perspective.

Figure 13 shows the development of a partial immersion behind the drop front with a comparison of lateral ($We = 162$, $\alpha = 29.2°$) and vertical perspective ($We = 131$, $\alpha = 29.8°$). In lateral perspective a lamella appears at $\tau = 0.9$ at the drop front. At $\tau = 1.0$, the vertical appearance of the drop and its surrounding lamella is perfectly circular. This means that the lamella either develops completely around the contact line, but is situated beneath the surface in the rear part as it is invisible in lateral view, or there is simply a depression at the rear part of the same size as the lamella, both together producing a circular black zone in vertical view. At $\tau = 1.8$, the zenith of the drop has almost disappeared in lateral view, and in vertical view, a faint white circular line appears in the front part of the black zone, which is presumably a shallow valley around part of the drop fluid forming a hemisphere. The outline of the black zone at $\tau = 2.0$ is still almost perfectly circular, only the rear part is slightly ellipsoidal.

An abrupt change can be seen in comparing the vertical view at $\tau = 3.0$ with that at 2.0: the black zone is no longer circular, instead there is a protrusion at the front, and at the sides, surface waves detached from the black zone appear. In lateral view, a step occurs in the front part of the drop contour at $\tau = 3.2$ which becomes even more pronounced at $4.1 \leqslant \tau \leqslant 5.9$. We interpret the three mentioned phenomena

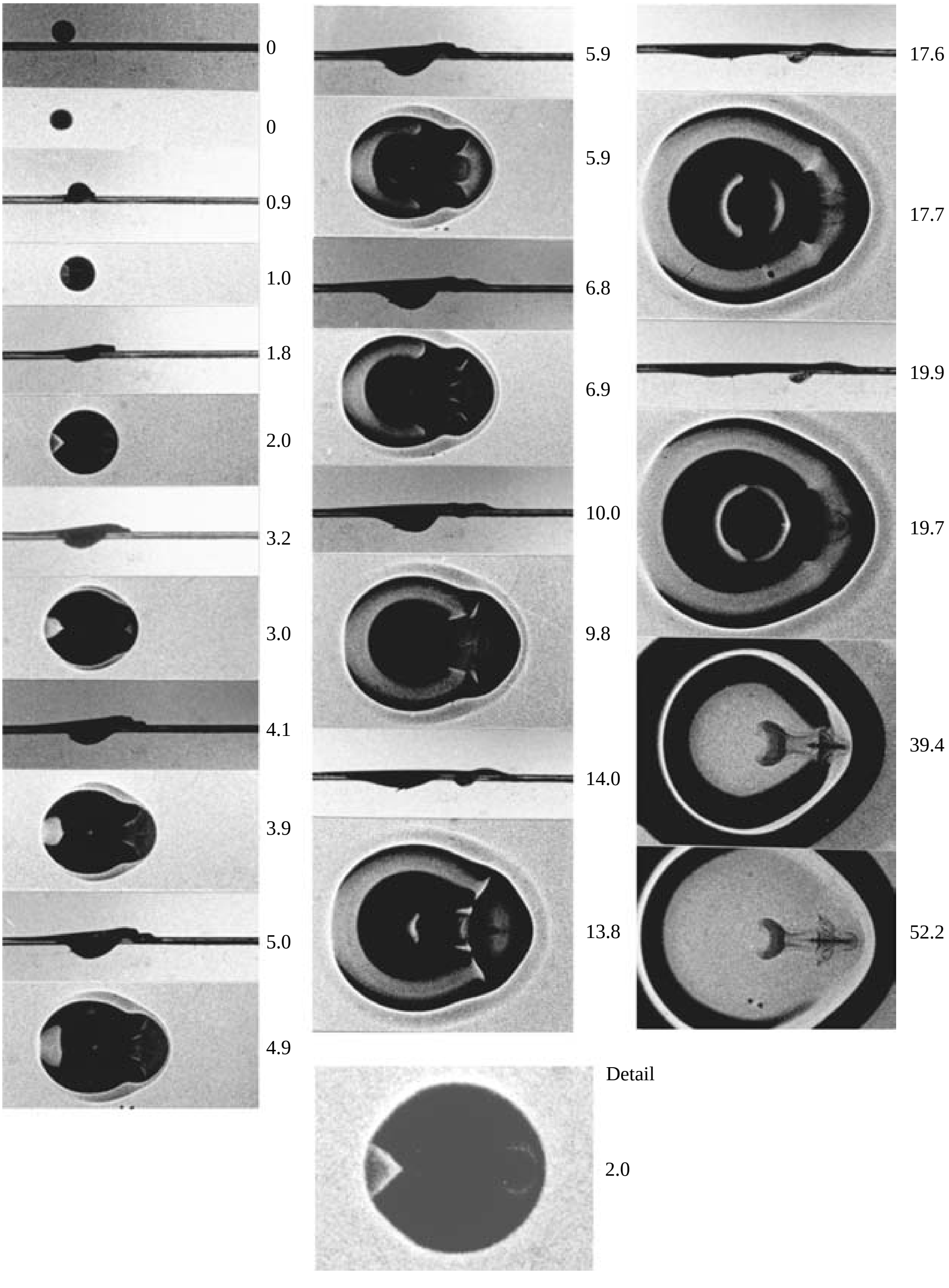

FIGURE 13. Partial immersion of drop fluid behind the drop front: comparison of lateral and vertical perspective. Lateral perspective: $\alpha = 29.2°$; $D = 2.0\,\mathrm{mm}$; $u_i = 2.15\,\mathrm{m\,s^{-1}}$; $We = 162$; $We_N = 38.4$; $Re = 430$; $Fr = 236$; vertical perspective: $\alpha = 29.8°$; $D = 1.9\,\mathrm{mm}$; $u_i = 1.99\,\mathrm{m\,s^{-1}}$; $We = 131$; $We_N = 32.5$; $Re = 378$; $Fr = 212$. Numbers on the right-hand sides of the visualizations reflect dimensionless time τ after impact.

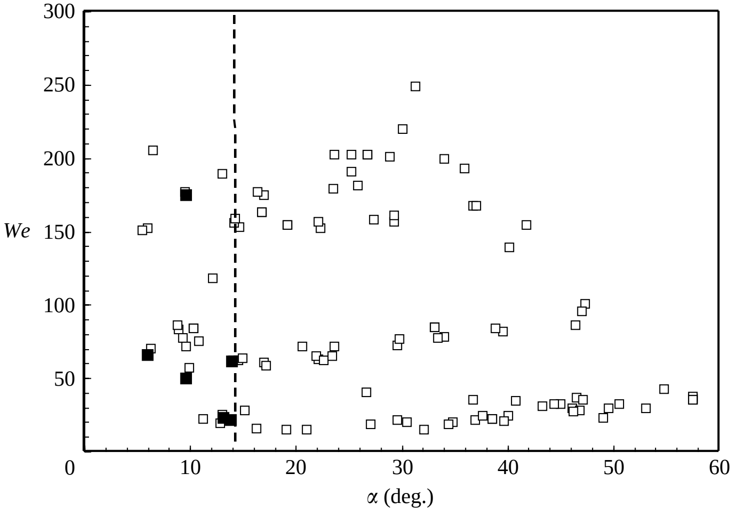

FIGURE 14. Regimes for rebounding (■) or permanent coalescence (□) for impacts of single drops.

(protruding drop front and the detached surface waves in vertical view and the step in the contour in lateral view) to be caused by an interaction of drop fluid with the lamella. We assume that part of the drop fluid (seen as a small hemisphere at $\tau = 2.0$) has still preserved momentum whereas the lamella (consisting of drop and target fluid, see § 3.8) has come to rest at $\tau = 3.0$. If this is the case, the drop fluid has to penetrate the lamella, which would explain the mentioned three phenomena.

The step in the contour in lateral view being visible for $3.2 \leqslant \tau \leqslant 6.8$ is succeeded by the partial immersion of drop fluid developing in this region when the step gradually disappears. When the localization of the step is compared to the vertical views, it becomes obvious that this 'step' is a complex three-dimensional wave structure; the troughs of these waves can be recognized as white lines in the black zone. The correspondence of these waves with partial immersion of drop fluid is discussed in § 4.

3.7. *Rebounding*

In figure 14, the regimes for coalescence and rebounding of single drops in the (α, *We*)-plane are shown. Here, 'rebounding' means that the drops first coalesce with the target surface, start spreading, but then contract and take off. As the drop diameter is of about the same size after rebounding, only small amounts of drop fluid are presumably left on the target surface. As can be seen, there are only six impacts where rebounding takes place (filled squares). In most cases, the drop coalesces permanently without rebounding (open squares). Permanent coalescence is found in the full parameter range studied with single drops without exclusion, whereas rebounding only occurs for $\alpha < 14°$ in the full *We*-range under consideration. There is no explanation at hand as to how this type of rebounding occurs, since there are impacts with permanent coalescence for almost identical parameters. Possible influences could be surface contaminations or strong drop oscillations before impact.

3.8. *Lamella formation: comparison of experimental and numerical results*

Figure 15 shows a comparison of experimental and numerical results for vertical, i.e. axisymmetric impact in the first stages after coalescence for $We = We_N = 177$. As

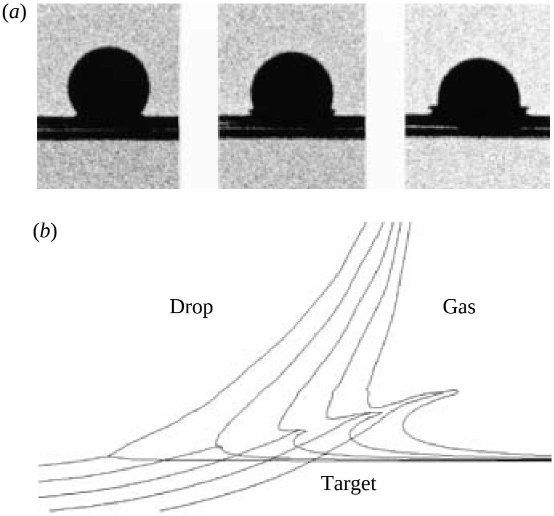

FIGURE 15. Lamella formation in vertical impact. (*a*) Experimental visualization for $D = 2.4\,\mathrm{mm}$; $u_i = 2.07\,\mathrm{m\,s^{-1}}$; $We = We_N = 177$; $Re = 497$; $Fr = 182$. Three time steps after impact are shown: $\tau = 0.13$; 0.21; 0.29. (*b*) Numerical simulation of vertical (axisymmetric) drop impact using the volume of fluid method of the commercial CFD-programme FLUENT 6.0. Surface tension is ignored, thus $We = We_N = \infty$, whereas viscosity is taken into account. Other impact parameters are identical to figure 15(*a*), i.e. fluid density $\rho = 1157\,\mathrm{kg\,m^{-3}}$ and fluid viscosity $\upsilon = 10\,\mathrm{mm^2\,s^{-1}}$ for both drop and target fluid; atmospheric pressure of gas phase: 1013 hPa; gas density: $1.2\,\mathrm{kg\,m^{-3}}$. Five time steps after impact are shown: $\tau = 0.07$; 0.11; 0.18; 0.21; 0.24.

can be seen, experiment and numerics agree qualitatively. The evolution of lamella formation is slightly advanced in the simulation copmared to the experiment, maybe because surface tension is omitted in the numerics.

As can be seen in figure 15(*b*), the lamella, which is pressed out at the contact line of drop and target fluid consists of both fluids with the larger mass fraction coming from the target fluid. Thus, the simulation supports the conclusion drawn in § 3.4 that the outer surrounding line in the vertical views of the spread drop fluid is generated by lamella formation in the first stage of impact.

4. Discussion

Three dominant phenomena leading to the spectrum of morphological patterns deserve to be discussed: (i) the transition from a capillary wave to lamella ejection at $We_N = 10$ in the initial stage after impact; (ii) the partial immersion of drop fluid at the rear part of the crater; (iii) the partial immersion at the drop front.

We will first focus our attention on the transition at $We_N = 10$. This phenomenon was studied numerically by Weiss & Yarin (1999) who named the capillary waves propagating on the drop and target fluid with the term 'neck distortion' and the lamella as 'jetting'. Weiss & Yarin (1999) studied the evolution of vertical drop impact onto a thin liquid film with the drop being already in contact with the target fluid in a finite contact zone as starting condition and a toroidal surface contour at the contact line to avoid surface tension singularities. They estimated that acoustic waves have no measurable effect for low Mach numbers $Ma = u_i/c = O(10^{-3})$ and therefore omitted fluid compressibility. In the boundary integral method that they used, viscosity was also neglected, but surface tension was taken into account and solutions are presented for the Weber numbers 2, 10, 40, 200, 1000 and infinitely large (when surface tension was omitted) up to a time after impact $\tau = 0.0015$ (in our definition). In their figure 8, they show that a gradual transition takes place from capillary waves which can clearly be seen for $We = 2$ to a jet or lamella that forms for $We = 200$. They estimate that the transition between the two phenomena takes place at $We \approx 40$, but this can only be taken as a rough estimate since they did not study the evolution of the contour for times after impact $\tau > 0.0015$.

Weiss & Yarin (1999) conclude that jetting (= lamella formation) occurs when the pressure rise in the contact area of drop and target fluid (owing to the stagnation pressure $p_s = \rho u_i^2/2$) exceeds the pressure decrease produced by surface tension due to the concave curvature in the 'neck' at the contact line. In this case, fluid is pressed out in the contact zone forming a thin sheet or lamella. In the other case, when surface tension dominates, fluid is sucked into the neck region by the pressure decrease and the initial abruptness of this process forms capillary waves on both surfaces. The authors therefore further conclude that the Weber number is the appropriate parameter to describe this transition. Lamella formation in the neck region was also studied analytically and numerically by Josserand & Zaleski (2003). Unfortunately, they only show results for $We = 8000$, which does not allow us to draw conclusions for the transition from capillary waves to lamella ejection.

We are not aware of any experimental description of capillary wave or lamella formation due to drop impact, although the phenomena can also be found on the visualizations of other authors. Qian & Law (1997) studied binary droplet collisions at different We and impact angles. On the photographs shown in their figure 4 it can be seen that for near head-on collisions up to $We_N = 4.9$ (value of We_N in our definition), a capillary wave appears on both drop contours, whereas for $We_N \geqslant 8.2$, lamella ejection takes place similar to that shown here in figures 2(*b*) and 2(*c*), respectively. When comparing their visualizations to the present ones, it has to be taken into account that they form the Weber number with the relative velocity of the two drops, which corresponds to $2u_i$ for our experiments, thus the Weber numbers given by them have to be divided by 4 to compare with our We numbers. We assume that Qian & Law (1997) were not aware of the transition in surface contours since they do not comment on the phenomena. Anyhow, we appreciate their visualizations as a second experimental confirmation of our discrimination between capillary wave or lamella formation.

For a quantitative comparison of the transition Weber number, it has to be taken into account that the surface contour of a drop impacting on a plane liquid differs from that of binary drop impact. Owing to the explanation given by Weiss & Yarin (1999) of the balance of surface to inertial forces it has to be expected that the transition occurs at lower We_N for binary drop collisions than for impacts on plane surfaces. Therefore, we conclude that the two critical Weber numbers $We_N \approx 6.5$ and 10, respectively, are not to be seen as a deviation; instead they support each other. Further, we assume that the estimate given by Weiss & Yarin (1999) would become more accurate if further time steps and viscosity were taken into account.

In the case of lamella ejection, our experiments can be compared to the normal impact of a large drop ($D \approx 6\,\mathrm{mm}$) on a fluid layer studied by Thoroddsen (2002) who shows that the lamella mainly consists of target fluid in the periphery of the drop where it forms a very thin sheet (see his figure 4). The ejecta sheet shown there is produced with impact parameters $We = We_N = 3257$ and $Re = Re_N = 9100$ so that the parameters differ by a factor of approximately 100 from ours. Our numerical results shown in figure 15(*b*) are in agreement with the findings of Thoroddsen (2002) since the tip of the lamella only consists of target fluid.

We will now consider the partial immersion of drop fluid at the rear part of the crater. When drop fluid mixes into target fluid, there has to be a velocity component normal to the interface of the two fluids which cannot be produced directly by the inertia of the drop, since the stagnation pressure leads to velocity components tangential to the interface as can be seen from lamella formation discussed above and shown in figure 15. As will be shown below, vorticity is produced at the free surface in the vicinity of the contact line. It seems to be probable that when a rear immersion forms, vorticity separates from the boundary layer where it was generated and advects drop fluid into target fluid.

There are several publications dealing with vorticity generation in vertical drop impact (see e.g. Peck & Sigurdson 1994; Cresswell & Morton 1995). The latter try to explain why vortex rings are formed for $We < 64$ as found by Hsiao, Lichter & Quintero (1988). As deduced by Batchelor (1967), vorticity can only be produced at solid boundaries or free surfaces, not in the bulk of a homogeneous fluid between shear layers. For vorticity production at a free surface, this surface must be curved because the amount of vorticity $\Delta\omega$ is given by

$$\Delta\omega = (2\kappa q)_{free\ surface}, \tag{1}$$

where κ is the curvature of the surface and q its tangential velocity component (see Batchelor, § 5.14). Cresswell & Morton (1995) estimate the vorticity generated in the neck region of the contact line of both fluids and conclude that it is of the same order of magnitude as that of the vortex ring that becomes visible.

As there are no theoretical results on inclined drop impact and vorticity generation available so far, we make an estimate of the vorticity produced at the rear contact point ω_{rp}, i.e. the rear intersection point of the plane of symmetry of the drop and the circumference of the contact zone (see figure 16*a*). Unfortunately, we cannot make use of (1) directly since we are unable to estimate adequately the curvature $\kappa(t)$ of the surface; therefore, we neglect both surface tension and lamella formation and reduce our estimate to a simple geometrical consideration. We take into account the fact stated in (1) that to produce vorticity at a free surface there has to be a tangential surface velocity q. The tangential velocity on the drop surface will be directed towards the rear point as long as the drop is only immersed with its lower hemisphere. Consequently, the velocity on the target surface has to be directed away from the rear point when vorticity is to be produced in this region. Owing to immersion of the spherical drop, target fluid is displaced; this happens with the propagation velocity of the rear contact point u_{rp}, which is sketched in figure 16(*a*):

$$u_{rp} = \frac{u_{iN}}{\tan\beta} = u_{iN}\frac{1-2\tau_N}{2\sqrt{\tau_N(1-\tau_N)}} \text{ with } \tau_N := \frac{u_{iN}t}{D}. \tag{2}$$

The surface velocity on the target fluid is directed away from the rear point as long as $u_{rp} > u_{iT}$. As long as this relation holds, vorticity is produced in the vicinity of the rear point; the respective time interval $\Delta\tau$ is given by:

$$\Delta\tau = \frac{1-\sqrt{1-\sin^2\alpha}}{2\sin\alpha}. \tag{3}$$

$\Delta\tau$is shown in figure 16(*c*) for $0 \leqslant \alpha \leqslant 90°$. $\Delta\tau\ (\alpha = 90°) = 0.5$ means that in the case of vertical impact, vorticity is produced at the free surface as long as drop penetration has not reached the equator of the drop.

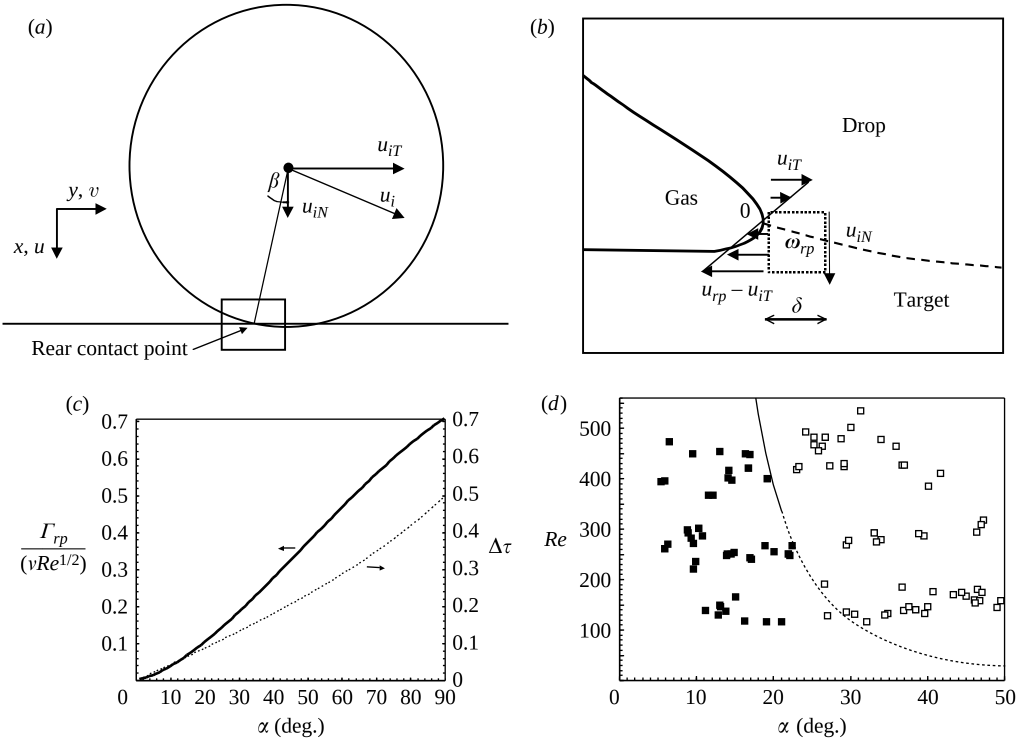

FIGURE 16. Estimate of vorticity generation for partial immersion at the rear part of the crater. (*a*) Sketch of geometry in the plane of symmetry of the impacting drop. (*b*) Sketch of estimated velocity field in the vicinity of the rear point. (*c*) Vorticity $\Gamma_{rp}/(\nu Re^{1/2})$ and time interval $\Delta\tau$ *vs.* α. Solid line: Γ_{rp} as given in (5); dashed line: $\Delta\tau$ as given in (3). (*d*) Regimes of partial immersion of drop fluid at the crater rear in the (α, Re)-plane. ■, no immersion; □, immersion as shown in figure 4(*c*). The curve represents (5) with $\Gamma_{rp}/\nu = 2.0$ being fitted to the experimental data. Solid part of curve is in the range $We > 100$, dashed part of curve $We < 100$; (5) was derived for $We \gg 1$.

As illustrated in figure 16(*b*), we estimate the vorticity generation in the vicinity of the rear point to be:

$$\omega_{rp} = \frac{\partial u}{\partial y} - \frac{\partial v}{\partial x} \approx \frac{\Delta u}{\delta} - \frac{\Delta v}{\delta} = \frac{(u_{iN} - 0)}{\delta} - \frac{(-(u_{rp} - u_{iT}) - 0)}{\delta} = \frac{u_{iN} + (u_{rp} - u_{iT})}{\delta}, \tag{4}$$

where δ is the thickness of the boundary layer at the contact line, which is estimated to be $\delta \approx \sqrt{\nu t}$.

The contribution of the tangential velocity gradient $\partial v/\partial x$ vanishes for $u_{rp} = u_{iT}$. To estimate the effect of the impact angle on vorticity formation we calculate the circulation Γ_{rp} in the vicinity of the rear point after the time interval $\Delta\tau$ with $\delta = \sqrt{\nu \Delta\tau D/u_i}$:

$$\Gamma_{rp}/\nu = \frac{1}{\nu}\oint_C \boldsymbol{u}\cdot \mathrm{d}\boldsymbol{l} = \frac{1}{\nu}\int_A \boldsymbol{\omega}_{rp}\cdot \mathrm{d}\boldsymbol{A} \approx \frac{1}{\nu}\int_A (u_{iN}/\delta)\,\mathrm{d}\boldsymbol{A} = \frac{1}{\nu}\delta u_{iN} = \sqrt{Re\Delta\tau}\sin\alpha. \tag{5}$$

The dependence of $\Gamma_{rp}/(\nu Re^{1/2})$ on α is depicted in figure 16(*c*). We interpret (5) such that vorticity generation in the rear neck region in oblique impact must exceed a critical constant before the boundary layer formed at the free surface separates and advects vorticity into the bulk fluid which is followed by a partial immersion of drop fluid into the target fluid.

Since vorticity generation depends on *Re* (see (5)), we show the regime of partial immersion at the rear of the crater in a *Re vs.* α plot in figure 16(*d*). Open squares refer to impacts with an immersion, filled squares to those without. The curve represents (5) with the constant $\Gamma_{rp}/\nu = 2.0$ being fitted to the experimental data. As can be seen, the curve reasonably divides the parameter space into the experimentally found regimes. Only one data point showing immersion ($Re = 128$; $\alpha = 27°$) is outside the range delimited by (5). This might be because the estimate given with (5) was derived by omitting surface tension and becomes invalid for low *We*. As has been shown by Dooley *et al.* (1997), vortex rings form even for $We \ll 1$ with $\alpha = 90°$, so that there is no lower boundary in *Re* for vortex formation with $\alpha = 90°$. Therefore, (5) is represented as a solid curve for $We > 100$ and as dashed curve for $We < 100$ in figure 16(*d*).

The third phenomenon to be discussed is the partial immersion of drop fluid behind the front of the spreading drop. As already discussed for the rear immersion, to immerse drop fluid, vorticity has to be formed which can only occur at curved free surfaces with tangential velocity, see (1). It was described in § 3.6 that surface waves develop in the front range (see figure 13), most probably owing to the penetration of drop fluid through the lamella consisting of drop and target fluid. As the immersion in the front range appears exactly at the location where the surface waves decay, the correlation is evident.

The question remains why no immersion is formed for the parameter combination: $We < 50$ and $We_N > 10$. This could be explained with the proposed interaction of moving drop fluid with the lamella. Apparently the impact momentum is too low in the range $We < 50$ for the drop fluid to penetrate the lamella, so vorticity production is suppressed. What remains unexplained is the second front immersion type as shown in figure 8(*b*), of which too few examples exist to draw reasonable conclusions.

5. Conclusions

From the experimental results, the following conclusions may be drawn:

(i) In the studied (α, We) range, coalescence always takes place in the initial stage of contact of drop and target fluid.

(ii) Only for $\alpha < 14°$ do some drops rebound after initial coalescence and depression of the interface, with the rebounding drop being of the same size as the impacting drop. However, even in the range $\alpha < 14°$, most drops coalesce permanently. The mechanisms for rebounding after initial coalescence are unclear, but owing to the stochastic appearance of this impact outcome they seem to be connected with fluctuating boundary conditions.

(iii) In the initial stage after impact, convex capillary waves appear on the drop and target surface for $We_N < 10$. These waves propagate from the contact line at the drop front to the zenith of the drop contour and away from the contact line on the target surface.

(iv) For $We_N > 10$, no capillary waves can be seen. Instead, a lamella is ejected at the drop front which partially consists of drop fluid, but its larger fraction is target fluid, as was shown numerically. Because of lamella ejection, the spreading velocity of the drop exceeds the impact velocity u_i by a factor of 1.1 to 1.6 in the first stage after impact before it gradually decreases in the second stage.

(v) Conclusions (iii) and (iv) are in qualitative agreement with the numerical results presented by Weiss & Yarin (1999) who show that in the contact-line region, the balance of surface tension and inertial forces decides whether this region of high curvature is distorted by surface tension producing capillary waves or whether the stagnation pressure of the impact presses out a lamella. Our transition Weber number, $We \approx 10$, quantitatively agrees with the experimental visualizations shown by Qian & Law (1997), even though the authors do not comment on the phenomena.

(vi) For $We < 140$ and $\alpha < 23°$, the drop volume spreads on the target fluid surface with no visible immersion of drop fluid into the target fluid. Outside this range, a partial immersion of drop fluid can be seen, either in the rear part of the crater, or behind the front of the spreading drop, where two different types of partial immersion occur.

(vii) Empirically, the rear immersion was found for all impacts with $\alpha > 23°$. To explain the formation of the rear immersion, we considered the vorticity generation in the rear part of the contact-line region. In an estimate ignoring surface tension effects, the circulation in the vicinity of the rear point of the contact line is found to be: $\Gamma_{rp}/\nu \sim \sqrt{Re\Delta\tau}\sin\alpha$, where $\Delta\tau$ is the time interval during which $u_{rp} > u_{iT}$. It is found that the rear immersion occurs for all $\Gamma_{rp}/\nu \geqslant 2$. As the estimate was derived for $We \gg 1$, it becomes invalid for low We.

(viii) Immersions behind the front of the spreading drop seem to be generated by two different effects since they occur in two different parameter ranges: (*a*) either for $We_N > 10$ and $We > 50$; or (*b*) for $We > 140$ and $\alpha < 23°$. As there were too few examples of the second type, we only interpreted the generation of the first type. It only occurs in the regime where a lamella is ejected. Several phenomena led to the conclusion that the vorticity leading to immersion is produced when part of the drop fluid penetrates the lamella that has come to rest. Apparently, this penetration only occurs for $We > 50$. In some cases even both front immersion types play a role and lead to two or more separate partial immersions.

(ix) The spread drop volume forms patterns of high complexity and strong sensitivity to the impact conditions (We, α). In the parameter range of the present study, ten different types of pattern are found with impacts at similar parameters being morphologically similar so that pattern formation is proved to be reproducible.

(x) Transitions between the different types of pattern are discrete rather than continuous. The discrete steps in pattern formation are most probably a result of the threshold found for the lamella ejection at the contact line and the thresholds for partial immersions of drop fluid at the rear part of the crater or behind the drop front.

(xi) The tangential velocity component in oblique drop impact induces a velocity field in a boundary layer on the target surface. Once the relative motion between drop and target surface is zero, this velocity field slowly deforms the spread drop fluid.

(xii) Pattern formation in oblique drop impact thus has a discrete time structure with capillary waves or lamella ejection in the first stage, partial immersions connected with crater formation or the penetration of the lamella by the spreading drop in the second stage and the deformation of spreading drop fluid owing to the induced velocity field on the target surface in the third stage. So the impact creates wave motions and vorticity, which in some cases separates from the boundary layer to advect drop fluid into target fluid. When the waves have dissipated, slow convective motions induced in the target fluid remain.

It is a pleasure for us to express our gratitude to Professor C. Tropea, TU Darmstadt for his interest in and support for this investigation and to the referees for their valuable criticism and suggestions. Further, we would like to thank P. Wandrés, M. Engel, B. Gamm and S. Häusser for their excellent technical assistance. We gratefully acknowledge financial support from the Deutsche Forschungsgemeinschaft (Ro 311/16-1), the Software AG Stiftung, the Mahle Stiftung and the Rudolf Steiner–Fonds für Wissenschaftliche Forschung.

REFERENCES

Batchelor, G. K. 1967 *An Introduction to Fluid Dynamics.* Cambridge University Press.

Beard, K. V., Ochs, H. T. & Liu, S. 2001 Collisions between small precipitation drops. Part III: Laboratory measurements at reduced pressure. *J. Atmos. Sci.* **58**, 1395–1408.

Brauer, H. 1971 *Grundlagen der Einphasen- und Mehrphasenströmungen*, p. 200. Sauerländer.

Bussmann, M., Mostaghimi, J. & Chandra, S. 1999 On a three-dimensional volume tracking model of droplet impact. *Phys. Fluids* **11**, 1406–1417.

Ching, B., Golay, M. W. & Johnson, T. J. 1984 Droplet impacts upon liquid surfaces. *Science* **226**, 535–537.

Cresswell, R. W. & Morton, B. R. 1995 Drop-formed vortex rings – the generation of vorticity. *Phys. Fluids* **7**, 1363.

Dooley, B. S., Warncke, A. E., Gharib, M. & Tryggvason, G. 1997 Vortex ring generation due to the coalescence of a water drop at a free surface. *Exps. Fluids* **22**, 369–374.

Hsiao, M., Lichter, S. & Quintero, L. G. 1988 The critical Weber number for vortex and jet formation for drops impinging on a liquid pool. *Phys. Fluids* **31**, 3560–3562.

Jayaratne, O. W. & Mason, B. J. 1964 The coalescence and bouncing of water drops at an air/water interface. *Proc. R. Soc. Lond.* A **280**, 545–565.

Josserand, C. & Zaleski, S. 2003 Droplet splashing on a thin liquid film. *Phys. Fluids* **16**, 1650–1657.

Kang, B. S. & Lee, D. H. 2000 On the dynamic behavior of a liquid droplet impacting upon an inclined heated surface. *Exps. Fluids* **29**, 380–387.

Liow, J.-L. 2001 Splash formation by spherical drops. *J. Fluid Mech.* **427**, 73–105.

MacKay, G. D. M. & Mason, S. G. 1963 The gravity approach and coalescence of fluid drops at liquid interfaces. *Can. J. Chem. Engng* **41**, 203–211.

Manzello, S. L. & Yang, J. C. 2002 An experimental study of a water droplet impinging on a liquid surface. *Exps. Fluids* **32**, 580–589.

Morton, D., Rudman, M. & Liow, J.-L. 2000 An investigation of the flow regimes resulting from splashing drops. *Phys. Fluids* **12**, 747–763.

Peck, B. & Sigurdson, L. 1994 The three-dimensional vortex structure of an impacting water drop. *Phys. Fluids* **6**, 564–576.

Qian, J. & Law, C. K. 1997 Regimes of coalescence and separation in droplet collision. *J. Fluid Mech.* **331**, 59–80.

Rein, M. 1993 Phenomena of liquid drop impact on solid and liquid surfaces. *Fluid Dyn. Res.* **12**, 61–93.

Rein, M. 2002*a* Capillary effects at newly formed liquid–liquid contacts. *Phys. Fluids* **14**, 411–414.

Rein, M. 2002*b* *Drop–Surface Interactions.* CISM Courses and Lectures No. 456. Springer.

Reznik, S. N. & Yarin, A. L. 2002 Spreading of a viscous drop due to gravity and capillarity on a horizontal or an inclined dry wall. *Phys. Fluids* **14**, 118–132.

Rioboo, R., Marengo, M. & Tropea, C. 2002 Time evolution of liquid drop impact onto solid, dry surfaces. *Exps. Fluids* **33**, 112–124.

Roisman, I. V., Rioboo, R. & Tropea, C. 2002 Normal impact of a liquid drop on a dry surface: model for spreading and receding. *Proc. R. Soc. Lond.* A **458**, 1411–1430.

Roisman, I. V. & Tropea, C. 2002 Impact of a drop onto a wetted wall: description of crown formation and propagation. *J. Fluid Mech.* **472**, 373–397.

de Ruijter, M. J., De Coninck, J. & Oshanin, G. 1999 Droplet spreading: partial wetting regime revisited. *Langmuir* **15**, 2209–2216.

Schotland, R. M. 1960 Experimental results relating to the coalescence of water drops with water surfaces. *Disc. Faraday Soc.* **30**, 72–77.

Thoroddsen, S. T. 2002 The ejecta sheet generated by the impact of a drop. *J. Fluid Mech.* **451**, 373–381.

Wang, A. B. & Chen, C. C. 2000 Splashing impact of a single drop onto very thin liquid films. *Phys. Fluids* **12**, 2155–2158.

Weiss, D. A. & Yarin, A. L. 1999 Single drop impact onto liquid films: neck distortion, jetting, tiny bubble entrainment, and crown formation. *J. Fluid Mech.* **385**, 229–254.

Willis, K. D. & Orme, M. E. 2000 Experiments on the dynamics of droplet collisions in a vacuum. *Exps. Fluids* **29**, 347–358.

Yarin, A. L. & Weiss, D. A. 1995 Impact of drops on solid surfaces: self-similar capillary waves, and splashing as a new type of kinematic discontinuity. *J. Fluid Mech.* **283**, 141–173.

Zhbankova, S. L. & Kolpakov, A. V. 1990 Collision of water drops with a plane water surface. *Fluid Dyn.* **25**, 470–473.

Zhbankova, S. L. & Kolpakov, A. V. 1999 Experimental study of collisions of differently sized droplets. *Colloid J.* **61**, 390–393.